DESIGN & INVESTIGATION OF DIFFERENT HIGHLY SENSITIVE PCF SENSORS BASED ON SURFACE PLASMON RESONANCE

by

Rahbar Al Rafid (170021126)
Shahriar Rashid (170021146)
Nausheen Zerin (170021070)

A Thesis Submitted to the Academic Faculty in Partial Fulfillment of the Requirements for the Degree of

BACHELOR OF SCIENCE IN ELECTRICAL AND ELECTRONIC ENGINEERING

Department of Electrical and Electronic Engineering
Islamic University of Technology (IUT)
Gazipur, Bangladesh

May 2022

DESIGN & INVESTIGATION OF DIFFERENT HIGHLY SENSITIVE PCF SENSORS BASED ON SURFACE PLASMON RESONANCE

Approved by:

18-5-22

Prof. Dr. Mohammad Rakibul Islam

Supervisor and Professor,
Head of the Department,
Department of Electrical and Electronic Engineering,
Islamic University of Technology,
Boardbazar, Gazipur-1704.

Date: ………………………………

Islamic University of Technology (IUT)

The Organization of Islamic Cooperation (OIC)
Gazipur-1704, Dhaka, Bangladesh
May-2022

Declaration

This is to certify that the project entitled “**DESIGN & INVESTIGATION OF DIFFERENT HIGHLY SENSITIVE PCF SENSORS BASED ON SURFACE PLASMON RESONANCE”** is supervised by Dr. Mohammad Rakibul Islam. This project work has not been Submitted anywhere for a degree.

…………………………….
Rahbar Al Rafid
ID: 170021126

shahriar Rashid
…………………………….
Shahriar Rashid
ID: 170021146

Nausheen zerin.
…………………………….
Nausheen Zerin
ID: 170021070

Table of Contents

Table of Contents .... **iii**

List of Tables .... **vi**

List of Figures .... **vii**

List of Equations .... **ix**

List of Acronyms .... **x**

List of Symbols .... **xiii**

Acknowledgements .... **xv**

Abstract .... **xvi**

Introduction to Optical Sensors **1**

1.1 A Brief History 1

1.2 Problem Description 4

1.3 Research Objective 5

1.4 Research Motivation 6

1.5 Thesis Framework 7

Photonic Crystal Fiber **9**

2.1 Introduction 9

2.2 Structure of PCF 10

2.3 Operation of PCF 12

2.3.1 The Bandgap Effect 13

2.3.2 Modified Total Internal Reflection 13

2.3.3 High Index Guiding Fibers 14

2.4 Fabrication of PCF 15

2.4.1 Capillaries Fabrication 16

2.4.2 Stacking 16

2.4.3 Drawing of PCF 17

Surface Plasmon Resonance **20**

3.1 Introduction 20

3.2 Working Principle 21

3.3 Literature Analysis 23

3.3.1 Surface Plasmon Wave 23
3.3.2 Surface Plasmon Polariton 24
3.3.3 Evanescent Field 26
3.4 SPR Advantages 27
3.5 SPR Applications 28
Photonic Crystal Fibers based on SPR 30
4.1 Introduction 30
4.2 Types of Sensing 31
4.3 Types of PCF Sensor Structures 33
4.3.1 D-Shaped Structure 33
4.3.2 Hexagonal Lattice Structure 35
4.3.3 Circular Lattice Structure 37
4.3.4 Trigonal Structures 38
4.3.5 Trapezoidal Structures 39
4.3.6 Square Structures 40
4.3.7 Spiral Structures 41
4.4 Plasmonic Material on PCF 41
4.4.1 Gold 42
4.4.2 Silver 42
4.4.3 Copper 43
4.4.4 Aluminium 43
4.4.5 Transparent Confucting Oxides (TCO) 43
4.5 Dielectric Materials 44
4.5.1 Silica 44
4.5.2 Air 45
4.6 Multianalyte Sensor 46
4.7 Analyte Classification 47
Proposed Design: Ultra-Sensitive SPR sensor for multipurpose sensing 48
5.1 Introduction 48
5.2 Schematic Modeling 49
5.3 Fundamental mode field profile 50
5.4 Dispersion and stacked preform 51

5.5 Gold (Au) and TiO_2 film thickness optimization 52
5.6 Pitch (p) and air hole diameters (d_1 & d_2) optimization 53
5.7 Analyte sensing of our proposed design 55
5.8 Temperature sensing of our proposed design 58
5.9 Magnetic field sensing of our proposed design 61
5.10 Methods of fabrication 64
5.11 Fabrication tolerance investigation 64
5.12 Explanation of improved performamce 65
5.13 Suitable analysis for sensing 67
5.14 Maintaining excellent performance 68
5.15 Recommendations for future research and improvement 69
5.16 Conclusion 70
Conclusion and Future work 71
6.1 Conclusion 71
6.2 Future work 71
References 73
Publication 87

List of Tables

Table 4.3.1 Comparison of D-shaped structure.. 34

Table 4.3.2 Comparison of Hexagonal structures 36

Table 4.3.3 Comparison of circular lattice structures 38

Table 5.7.1 Performance analysis of the proposed sensor with varying dielectric RI 56

Table 5.7.2 Comparison of different parameters between the proposed and other reported sensors 57

Table 5.8.1 Performance analysis of the proposed sensor with varying temperature. 60

Table 5.8.2 Comparison between the proposed temperature sensor and other reported sensors. 60

Table 5.9.1 Magnetic field sensing performance of the proposed sensor 63

Table 5.9.2 Comparison between the proposed magnetic field sensor and other reported sensors 63

List of Figures

fig. 1. 1 Schematic of a typical optical sensor 3

fig. 2. 1 Schematic of a typical optical sensor 10

fig. 2.2 Basic Types of Cores in PCF........ 11

fig. 2.3 Schematic of stack and draw method (a) Stacking of PCF preform (b) Drawing process of the fiber (c) PCF preform preparation 15

fig. 2.4 PCF preform connected with silica tube (a) Successful preform connection (b) Waist deformation 18

fig. 2.5 Cross-section of PCF at different stages (a) PCF preform (b) PCF Cane (c) PCF of 125 μm diameter (d) Microstructure around PCF core 19

fig. 3.1 The conventional SPR setup with working principle 22

fig. 3.2 Schematic of Surface Plasmon Polariton 25

fig. 3.3 (a) Kretschmann and (b) Otto configuration of an Attenuated Total Reflection setup for coupling surface plasmons. 26

fig. 3.4 Evanescent Field........ 27

fig. 4.1 Kretschmann Configuration of Prism based SPR sensor 31

fig. 4.2.1 (a) Internal Sensing structure (b) Loss curve 32

fig. 4.3.1.1 D shaped structure with hollow core 33

fig. 4.3.5 Trigonal Structured PCF........ 39

fig. 4.3.6 Trapezoidal channel-based PCF 40

fig. 4.3.7 Square lattice PCF design........ 40

fig. 4.3.8 Spiral Structured PCF sensor........ 41

fig. 5.1 (a) 2D Schematic cross section, (b) 3D Fiber tube........ 50

fig. 5.2 Fundamental mode field profile of core mode for (a) x-pol, (b) y-pol; and SPP mode for (c) x-pol, (d) y-pol........ 51

fig. 5.3 (a) Phase matching of x-polarization (b) Stacked preform structure 51

fig. 5.5 (a) CL curves for environment RI of 1.37 and 1.38 at tg = 15 nm, 20 nm, 25 nm (b) AS curves at tg = 15 nm, 20 nm, 25 nm (c) CL curves for environment RI of 1.37 and 1.38 at tt = 10 nm, 15 nm, 20 nm (d) AS curves at tt = 10 nm, 15 nm, 20 nm. 54

fig. 5.6 (a) CL curves for environment RI of 1.37 and 1.38 at p = 0.95 µm, 1.00 µm and 1.05 µm (b) AS curves at p = 0.95 µm, 1.00 µm and 1.05 µm (c) CL curves for environment RI of 1.37 and 1.38 at d1 = 0.90 µm, 0.85 µm and 0.80 µm (d) AS curves at d1 = 0.90 µm, ... 55

fig. 5.7 (a) CL curves for x-pol at analyte RI of 1.33 to 1.43 and (b) AS curves for x-pol at analyte RI of 1.33 to 1.42 at optimized parameters………………………………………………… 56

fig. 5.8 (a) CL curves for different temperatures; (b) Resonant Wavelength vs. Temperature curve for a range of -70 ◦C to 70 ◦C………………………………………………………………… 59

***fi*g. 5.9** (a) CL curves for different applied magnetic field intensities (b) Resonant Wavelength vs. Magnetic field strength in a range of 0 to 1000 Oe…………………………………………… 62

fig. 5.11 CL curves at analyte RI 1.37 with ±5% and ± 10% variation in (a) parameter d1, and (b) parameter d2. 67

fig. 5.12 Channel highlighted sensor structures of (a) this work, (b) ref.[91], (c) ref. [98], (d) ref.[99], (e) ref.[117], (f) ref.[93]. 69

fig. 5.13 Amplitude Sensitivity of different sensors vs. total channel angle. 70

List of Equations

Equation 1 - The feeding rate of preform & Tractor Drawing ………………………………16

Equation 2 -The dispersion relation for electronic & magnetic surface plasmons …………..21

Equation 3 - Relation between real and imaginary part of complex permittivity ……………23

Equation 4 - RI of Silica & Sellmeir Equation ……………………………………………….45

Equation 5 - The equation of ethanol's RI with temperature …………………………………55

Equation 6 - The temperature fitting curve …………………………………………………..58

Equation 7 - MF RI and the applied magnetic field …………………………………………61

Equation 8 - The magnetic field sensitivity …………………………………………………..61

Equation 9 - The magnetic fitting Curve ……………………………………………………..62

List of Acronyms

AI	Amplitude Interrogation
ALD	Atomic Layer Deposition
AS	Amplitude Sensitivity
ATR	Attenuated Total Reflection
AZO	Aluminium Doped Zinc Oxide
CL	Confinement Loss
CVD	Chemical Vapour Deposition
DNA	Deoxyribonucleic Acid
EM	Electro-Magnetic
EMI	Electromagnetic Interference
EML	Effective Material Loss
FBG	Fibre Braggs Grating
FEM	Finite Element Method
FOM	Figure of Merit

FWHM	Full Width Half Maximum
GZO	Gallium Doped Zinc Oxide
IR	Infra-Red
ITO	Indium Tin Oxide
LSPR	Localized Surface Plasmon Resonance
MF	Magnetic Fluid
PCF	Plasmonic Crystal Fibre
PML	Perfectly Matched Layer
PBG	Photonic Band Gap
QD	Quantum Dots
RI	Refractive Index
RIU	Refractive Index Unit
RNA	Ribonucleic Acid
RW	Resonant Wavelength
SP	Surface Plasmon
SPP	Surface Plasmon Polariton
SPR	Surface Plasmon Resonance

SPW	Surface Plasmonic Wave
TC-PQF	Trapezoidal Channel Photonic Quasi-Crystal Fiber
TE	Transverse Electric
TIR	Total Internal Reflection
TiO2	Titanium Dioxide
TiN	Titanium Nitride
TM	Transverse Magnetic
WS	Wavelength Sensitivity
WI	Wavelength Interrogation

List of Symbols

n_{eff}	Effective Refractive Index
n	Real Part of Effective Refractive Index
n_{silica}	Refractive Index of Silica without Strain
λ	Wavelength of Light
B_1	Sellmeier Constant
B_2	Sellmeier Constant
B_3	Sellmeier Constant
C_1	Sellmeier Constant
C_2	Sellmeier Constant
C_3	Sellmeier Constant
T	Temperature
α	Confinement Loss
k	Wavenumber
SA	Amplitude Sensitivity
$S\lambda$	Wavelength Sensitivity
R	Resolution
B	Birefringence

L	Sensor Length
ST	Temperature Sensitivity
p	Pitch
d	Diameter
h	Height
w	Width
t_{PML}	PML Thickness
t_a	Analyte Layer Thickness
t_g	Gold Layer Thickness
t_t	TiO_2 Layer Thickness
r_c	Radius of the Sensor Core
Λ	Distance between two air hole centers
a	Air Hole Center to Cluster Center Distance

Acknowledgements

All praise to the almighty Allah (SWT), for He, has kept us alive in this COVID-19 pandemic and given us the capability and opportunity to finish this work perfectly with extraordinary results. It would not have been possible for us to finish this work without His blessings. Secondly, our heartfelt gratitude goes to our honorable supervisor, Professor Dr Mohammad Rakibul Islam, for his continuous support, helpful attitude, and most importantly, his constant patience during the learning phases. Without his motivation and guidance, we could not have come this far. We are also grateful to all the teachers of the Electrical and Electronic Engineering Department for their helpful attitude, valuable suggestions, and constructive criticism during the research work. After that, thanks to all our family members for supporting us in every phase of our life. Finally, we want to convey our gratitude to all the seniors, and well-wishers who have helped us accomplish our goal.

Abstract

Many Researchers have proposed many designs on SPR based PCF sensors. This field is outgrowing very rapidly due to its label free, real time monitoring detection technique and all other applications. So, sensors with better performance are discovered and on the way to be discovered, The sensitivity and accuracy are quite high in SPR sensors and it has fabrication friendly size. But in case of higher sensitivity, complex structures and fabrication complications arrive. That is why designing a PCF sensor includes some goals & others need to be compromised. Studying many PCF sensors, our design was proposed for an improved sensing performance and detecting magnetic and temperature changes. Also, the target was so that this design can be practically implemented. We proposed a circular lattice structure with gold coating. It was surrounded with a thin PML layer & stack and draw method was adapted for easy fabrication. We optimized various parameters whichever gave the best results. In all cases we used COMSOL Multiphysics 5.3a and Matlab for our researched work. Amplitude Sensitivity (AS) of 7223.62 RIU^{-1} and wavelength sensitivity (WS) of 28500 RIU^{-1} was noted. The Sensor resolutions are 1.38×10^{-6} and 3.50×10^{-6} RIU for amplitude and wavelength respectively and the sensor has a FOM of 914 with an analyte sensing range from Refractive indices 1.33 to 1.42. Aside from this, the sensor can perform as a temperature sensor with a maximum temperature sensitivity of 1.25 nm/ °C and also as a magnetic field sensor with a maximum sensitivity of 0.16 nm/Oe. Thus, denoting the high sensing capabilities, this proposed sensor can prevail as a potential asset in the bio-detection field.

Chapter 1

Introduction to Optical Sensors

1.1 A Brief History

Biosensors' application field has grown exponentially in recent years as a result of their extensive and advanced research potential. Based on the signal transduction method, biosensors can be divided into six categories: mass, optical, magnetic, electrochemical, thermal, and micromechanical sensors. The most impressive inventions in sensing applications are optical sensors [1], [2]. Sensing through optically enabled fibers has been used in a variety of industries for the past 60 years to enhance and test the durability, safety, and efficiency of structures, automobiles, biomedical and medical devices, and more. Fiber Optical Sensor (FOS) has been able to expand its capabilities over the last five years to incorporate unexpected levels of data and sensing frequency across applications in energy, aerospace, and even medicine. This is assisting engineering enthusiasts in solving current problems and innovating to advance their designs. Fiber optic technology has a broad range of real-world applications today, as well as a broad range of future possibilities.

The first fiber optic sensor, which used free-space optics, was patented in the 1960s. Researchers succeeded in developing the very first intrinsic fiber optic sensors about ten years later. For obtaining reliable mechanical measurements, this enhancement provided incomparable engineering advantages over free space sensors. Free spatial optics rely on line of sight and can’t be installed in operating structures or automobiles, whereas fiber optics allows signals to be transmitted in the interior of a deployable medium. The fiber optic gyroscope, which was first commercialized in the 1980s, was one of the first applications of fiber optic sensors and has since become an important component in stabilization, pathfinding and navigational systems. The civil engineering industry began using myriads of fiber optic sensors to quantify temperature, pressure, strain, and other parameters in the early 1990s [3].

As shown in Error! Reference source not found., typically an optical sensor is made up of a light source that generates electromagnetic waves, a light sensing platform where interactions between two entities- light and substance take place, and a device that detects and accurately standardizes spectral shifts in EM waves when they interact with specific analytes. Finally, digital results are displayed in a screen. To obtain sensor produced results from target molecules, optical sensors typically adopt two basic methods: label-based and label-free methods. Fluorescence-based biosensors with multi-step detection protocols are included in label optical biosensors. This method also necessitates reagent additions and washing steps. However, it has some drawbacks, such as toxic waste, reduced efficiency, short-term stability, time-consuming, biomolecule degradation, and so on. Without the need for labeling, label-free technology can allow for real-time monitoring. Furthermore, this technique can generate a signal without the use of additional probes that carry labels to provide the signals. Label-free technology is maintained with SPR, resonant mirrors, and interferometers for increased accuracy and efficiency. Optical sensors based on SPR have been crucial in the development of fiber-optic communication [4] . Special transducers, such as SPR (surface plasmon resonance), gratings, interferometers, and refractometers, are used in optical devices. Resonance, reflection, fluorescence, refraction, phosphorescence, dispersion, infrared absorption, and Raman scattering are all types of optical sensors. Optical sensors for sensing chemical and biological analytes are an abruptly expanding field of research with applications in a wide range of fields, including medical diagnostics, food analysis, environmental monitoring, security, genomics, agriculture, production and proteomics [5].

Researchers have been drawn to SPR-based optical sensors due to their unique, out of ordinary, and well-established characteristics, such as high rigidity, compact probe design, and higher sensitivity. SPR sensors are being investigated in a variety of fields due to their advantageous behavior, including gas detection, monitoring of water quality, medical diagnostics, food safety monitoring, glucose inspection, real-time monitoring, biosensing, strain sensing, and temperature sensing [6]–[8] . The study of SPR-based biosensors began during 1983 when Liedberg et al. brought forward SPR biosensors in the domain of gas detection and biosensing [9] and presented the prism-coupling method. The point cross-examination technique is used in prism enabled SPR sensors. The prism-based SPR sensor, on the other hand, is insuffucient for use in remote sensing because it contains multiple optical and mechanical parts, making the sensor bulky in size. To overcome these limitations, scientists have put fiber instead of prism, which has collected popularity due to its promising characteristics such as endless single-mode behavior, atypical dispersion, high nonlinearity, label-free detection, increased integrity, adjustable high birefringence, and portability.

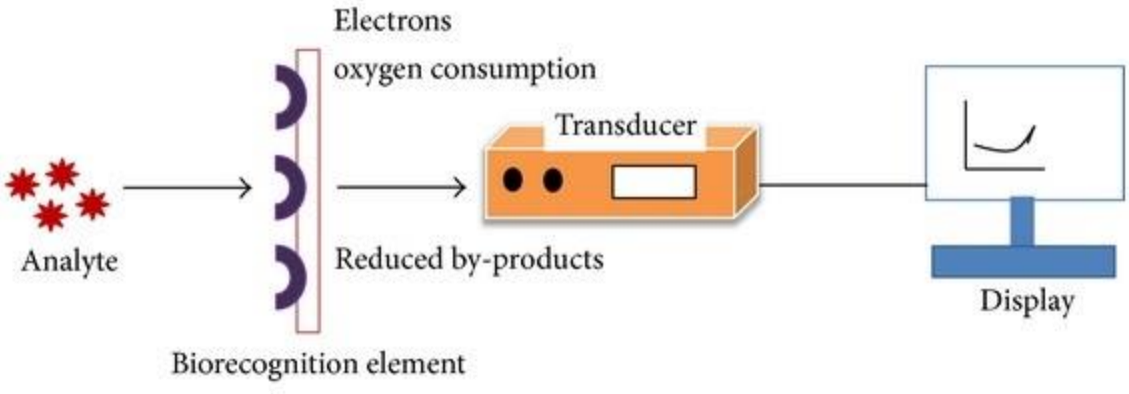

fig. 1.1 *Schematic of a typical optical sensor*

The incident of electrons' united oscillation at the metal and dielectric interface [10] causes surface plasmons, which are defined as the rise of the quantized transverse magnetic (TM) p-polarized electromagnetic wave. Surface plasmon resonance occurs when the incident wave's wave vector and the surface plasmon's wave vector match [11]. SPR is caused when a transverse magnetic wave strikes the metal-dielectric contact and excites the electrons inside it. As a result, the core-cladding region develops and circulates surface plasmon waves (SPW). In this case, the leaky core mode couples with the surface plasmon polariton (SPP) mode at a specific wavelength. The resonance wavelength (RW) is the name given to this specific wavelength, and the phase-matching condition is the name given to this phenomenon [12] . It has greater sensitivity and a smaller resonant peak than previous fiber-based sensors that have been reported [13]–[15] which results in unparalleled preciseness when discovering an unspecified substance or analyte.

1.2 Problem Description

Researchers have been paying close attention to SPR sensors because of their suitability for specific sensing applications and promising characteristics. Several optical sensors based on SPR techniques have been investigated to date. In general, the sensors use two types of sensing mechanisms. The internally metal-coated PCF sensor is the most common type, with the metal film coated internally [16]. This mechanism has some drawbacks, such as the time it takes to empty and refill the fiber. Furthermore, the internally coated layer is extremely delicate, making fabrication and structure extremely difficult. It also necessitates additional steps and maintenance in order to function properly, making it unsuitable for simpler sensing. To reduce the impediments, a D-shaped PCF sensor with improved structure is suggested. However, the fabrication of this type of sensor is more difficult [17] . To achieve an accurate result, the flat portion requires perfect polishing, making the fabrication process even more difficult and costly. The externally metal-coated PCF is a modern sensing approach in which the metal coating is placed outside the fiber. Gold, AZO, silver, aluminum, and other plasmonic materials are commonly used in these sensing processes. Because of the aqueous environment, most plasmonic materials oxidize, resulting in a decrease in sensing accuracy [18] . The fabrication complexity of the sensor, as well as its costing, can be increased based on the placement and size of the air holes. Also, geometrical pattern can also affect the fabrication error probability. More complex a design is, more error can occur in practical realization. Again, depending on error in implementation and geometry, sensitivity is affected. Many sensors have been reported to have lower sensitivity. Therefore, researchers are continuously trying to come up with a design that will maximize AS and WS while keeping the other drawbacks in check. To summarize, the following are the barriers of previously reported SPR-based sensors:

1. Inaccuracy in sensing
2. Fabrication hardships
3. Increased confinement loss
4. Weak evanescent field
5. Unprofitable costing

Thus, Moving forward, our motive was to design and test a design that will compensate most of the drawbacks mentioned above.

1.3 Research Objective

The predominant goal of our study was to design and investigate the impact of novel and unique PCF biosensors based on SPR. The following are the research's specific objectives:

1. To determine amplitude sensitivity (AS) and maximize it
2. To determine amplitude sensitivity (AS) and maximize it
3. Conducting a comprehensive literature review on SPR sensors.
4. Changing the thickness of different fiber layers, such as gold, titanium dioxide (TiO2), and analyte, allows for simulation of various parameters.
5. Use of different plasmonic materials to improve detection accuracy and performance of the PCF structure.
6. Investigation of performance and graphical results as a result of small changes in various parameters.
7. Optimize the geometrical parameters of the fiber
8. Find multifarious application of the developed sensor
9. Maximize sensor performing parameters- Figure of Merit and Sensor Resolution
10. Analyse real-life fabrication process of sensor and effects of associated errors
11. Compare our proposed PCF-SPR sensors with those published in other journals

1.4 Research Motivation

Researchers have been interested in PCF enabled sensors based on SPR technology because of their advantageous characteristics. The evanescent field, which is directed towards the coating region through the core, causes the freely moving electrons to move around and oscillate, and SPW is formed along the metal-dielectric surface, determines the sensitivity of this type of sensor. When this happens, the phase matching situation occurs, making it reliant on even minor changes in analyte RI. The fluctuations of RW are determined and further observed in a graphical form as RI changes.

SPR is regarded as a field that has yet to be fully explored. This industry has a great deal of room for improvement. As a result, scientists are still working to make it as useful as possible. These biosensors provide highly sensitive, compact, and high-frequency monitoring without the need for time-consuming sample pre-treatment. Also, more and more research are being conducted to simplify the fabrication process of these sensors. The development of stack and draw method is one of the finest steps taken in this direction. These sensors' applications range from biochemical and biotechnological fields to healthcare, security, and other areas. As can be seen, this technique is extremely versatile and has a broad range of applications. And thus, proper attention should be paid to the development of this technology. This sensor has a well-established analysis method that can produce accurate results in a matter of minutes, whereas previous laboratory sensors were very delicate, time-consuming, bulky and expensive to maintain. These biosensors can also be used to test bacteria, viruses, antibody-antigen, DNA, mRNA, RNA, hormones, hemoglobin, and protein, among other things.

Considering upcoming research opportunities, SPR sensors have shown an advantageous behavior which makes it a clear choice to further use it in the near future in electronics, physics, medical analyses, and software. Thus, at present, SPR is labeled as the most promising field to research.

1.5 Thesis Framework

This thesis book consists of 6 distinct chapters. Each of the chapter focuses on different topics related to our thesis. The gist of all the chapters has been summarized in this framework.

Chapter 2 presents an elaboration on photonic crystal fibers (PCF) and different classifications of it. The background history, development timeframe etc. has also been briefly discussed. The superiority of PCF compared to other techniques is detailed here. Most importantly the structure and fabrication process has been discussed in details in this part.

Chapter 3 tells us in details about the Surface Plasmon Resonance (SPR) phenomenon. How this detection method surpasses other detection methods, the working principle based on which it works, the essential components of it, advantages and applications have been conversed about.

Chapter 4 focuses on the PCF sensors that have been developed exploiting the SPR phenomenon. This type of sensor adopts a numerous method of sensing. All have been discussed in this section. Also, we discussed different structures of the sensor, how they differ with each other and how they have been reported in different literatures etc. A thorough analysis on different plasmonic materials have also been done in this chapter. This will help the readers understand why certain materials were used in the proposed sensors in future chapters.

Chapter 5 begins with the introduction of our proposed sensors and the final results of the simulation of that sensor. How the sensor was modelled, what method was used, what were the simulation parameters, all have been discussed in this chapter. Later we dive deep into the parameter optimization. Finding the ideal film thickness of the plasmonic materials, pitch, air hole diameters etc. has been done here. The relevant graph-shapes are also displayed here for reader convenience. We then discussed the analyte sensing performance of our proposed sensor. The parameters like confinement loss, amplitude sensitivity, wavelength sensitivity etc. has come up in this chapter and their graph-shapes has been plotted against the Refractive Index (RI) of the analyte. All numerical have been summarized at **Table 5.7.2** Comparison of different parameters between the proposed and other reported sensors. Our later section goes beyond our usual analysis and discussed as how temperature sensing can be done by our proposed sensor. The confinement losses and temperature ranges have been analyzed here and satisfactory results have been achieved.

This has been consolidated more in **Table 5.8.4** Comparison between the proposed temperature sensor and other reported sensors.where our sensor has been compared against other reported sensors. We presented another alternative sensing ability of our proposed sensor- magnetic field sensing. Here also, the necessary parameters have been analyzed and checked how well magnetic field sensing this sensor is able to do. Another comparison table comes up to consolidate the claim. The next section focused on the fabrication method of the proposed sensor. The fabrication tolerance has been included in this chapter. As we know, sensors tend to act differently when practical implementational errors are taken into consideration. This perspective has been explored here. Section 5.12 discussed the areas of improvement of our proposed design and how a comparatively unused parameter called ‘sensing angle’ can add new perspective to sensor developments in general. Types of analyte, ways to maintain excellent performance and recommendations have been imprinted in this section.

Chapter 6 is the final chapter of this book. This chapter gave a conclusion about our whole research and talked about future works.

Chapter 2

Photonic Crystal Fiber

2.1 Introduction

Environmental monitoring, industry, healthcare, food preservation, and other fields could benefit from photonic crystal fiber sensors. Flexible and upgraded photonic crystal fiber (PCF) constructions, controlled light propagation for spectral amplitude, phase, polarization, and wavelength measurement, and PCF-enabled interferometry techniques are used in these sensors. Based on published works, a few PCF-based physical sensors are encapsulated in this research book. On the basis of liquid infiltrated structures, solid core and hollow core structures, dual-core fibers, metal-coated fibers, and grating included fibers, some physical PCF sensors are explored. As sensing technology progresses, the possibilities of temperature, pressure, strain, twist, curvature, electromagnetic field, and refractive index sensing are also explored.

Compared to standard optical fiber, PCF has better geometry. PCF typically has a hollow or solid core surrounding which the air holes are spread in various decorations. The distribution of these air holes guides light. Changes in the pattern of air holes, as well as changes in the environment, can affect light propagation [19]. Over the last two decades, PCF's unique nature has attracted a lot of researchers for its sensing utilizations. In lieu of their high sensitivity, flexibility, robustness, minute size, and ability to be used in a variety of disadvantageous circumstances, PCF-based sensors have become the focus of numerous research groups. PCF-based sensing probes are easy to attach or insert into a system due to their small physical dimensions. Without the use of wires, these sensing probes can be attached electrically to the control setup. They can be used for remote sensing in hazardous and noisy environments, as well as high temperatures, high electromagnetic fields, and highly combustible environments.

2.2 Structure of PCF

Photonic crystal fibers (PCF) were created with the intention of guiding light in optical communicational system. A PCF is a particularly fabricated fiber with a refractive index that varies recurrently across the material [20]. The fiber is generally of silica construction, although, other materials have been tested. There is a core in the middle (can be on the sides as well) and an array of decoratively structured air holes or channels within the fabricated fiber. The guided waveform receives cladding insulation from the open channels surrounding the solid core PCF during transmission, confining the light in the core and ensuring that no light is lost during transmission [21]. The light is trapped to the core by Bragg reflection phenomena [20] or by total internal reflection [21]. Photonic Crystal Fiber is an almost lossless dielectric medium made up of a decorative pattern of microscopic air holes that runs the length of the fiber [22]. PCF traps light in its core, providing a better waveguide for photons than standard optical fiber. A solid silica core in PCF provides the optical signal's core guiding. This core is surrounded by a recurring air-hole order in the cladding. The light signal can be commanded by total internal reflection along with the silica defect core because the effective cladding index is lower than the core refractive index. The air holes add up to the low index cladding, and the core is usually formed by enlarging an

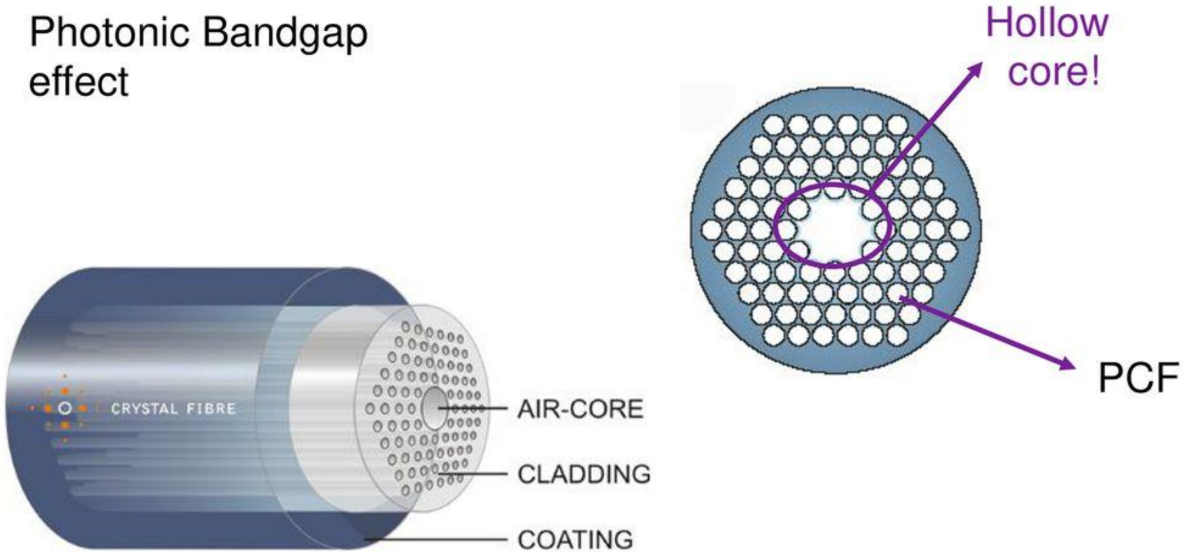

fig. 2.1 *Schematic of a typical optical sensor*

existing air hole or removing one from the structure's center. A typical photonic crystal fiber can be seen in Error! Reference source not found.**.** PCFs have some design flexibility, such as core r adius, ring number, air hole parameter, and pitch (air hole to air hole distance). Because the guiding power of optical fibers are dependent on the refractive index, and the refractive index of PCFs is dependent on those design rules, it is possible to gain guiding properties by modulating these parameters [23].There are many different kinds of PCFs, that can be divided in four classes: solid-core (SC-PCF), hollow-core (HC-PCF), suspended-core, and Kagome lattice as shown in Error! Reference source not found.. In 1996, the first PCF with a solid core was reported, which was achieved by inaugurating a "defect" area throughout the central core. Later, the first hollow-core PCF was reported, in which a "low-index defect" prevented light from being guided by total internal reflection [24]. The goal of early PCF research was to create a photonic bandgap, which is basically a light filter that prevents the transmission of a specific frequency of light [25]. Because the hollow core was not supposed to be able to create the required photonic bandgap, the first PCFs had a solid core. Kagome lattice arrays and hollow cores have higher light transmission losses, which limits their use over lengthy distances. They have, however, been shown to be useful in usages that require a wide range of wavelengths [26]. The fiber can contribute a region of distinct refractive index and so generate a waveguide once the core has been loaded with a liquid sample for HC-PCF based analysis.

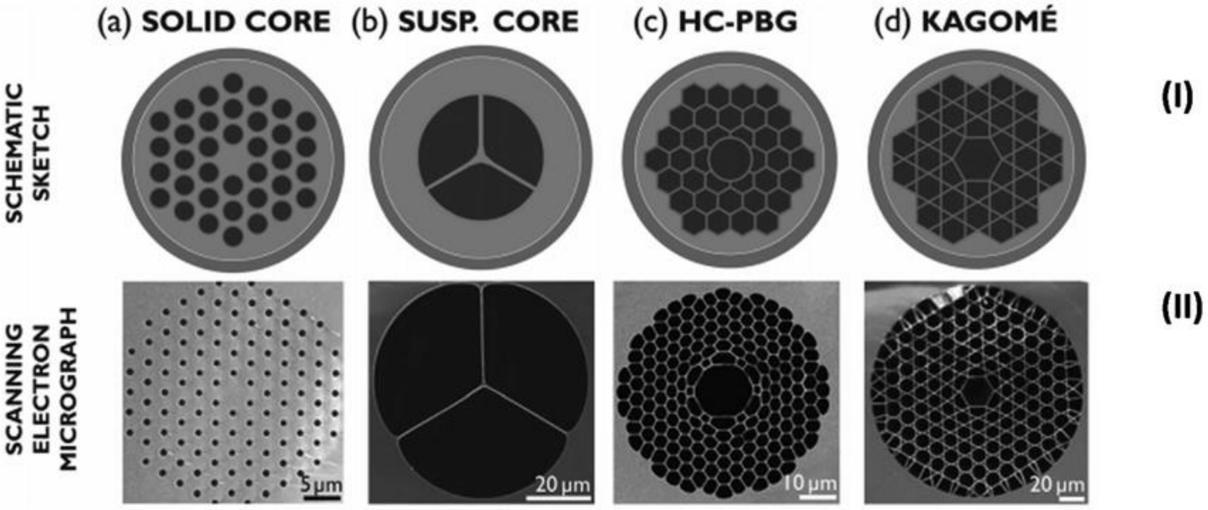

fig. 2.2 *Basic Types of Cores in PCF*

The structure of a PCF's core and cladding regions play an important role in its performance. J. Laegsgaard et al. proposed the honeycomb cladding structure first [27] . Following that, due to improved design flexibility and fabrication capabilities, a large number of designs have increased. Square [28], hexagonal [29], octagonal [30], spiral [31], circular [11], and hybrid [32] are some examples of well-implemented designs. In general, such fibers are made in the same way as other optical fibers: first, a centimeter-sized "preform" is made, and then the preform is heated and drawn down to an infinitesimally small diameter, shrinking the preform cross-section but keeping the same features. The preform at this stage can be compared to a human hair in real life. A single preform can produce kilometers of fiber in this manner. Although drilling/milling was used to create the initial aperiodic designs, stacking is regarded as the most commonly used method [33]. This served as the foundation for the development of the first soft glass and polymer fibers.

2.3 Operation of PCF

According to their confinement mechanism, photonic crystal fibers can be classified into two operational modes. Those consisting of a solid core, or a core with a higher average index than the micro structured cladding, can run on the same index-guiding principle as the traditional optical fibers. However, the effective refractive index contrast between the core and the cladding can be significantly larger. Thus, they can also have much robust confinement for nonlinear optical instruments, polarization-maintaining fibers, and other applications. Utilizing this, nonlinear electronics can be used to upconvert a weak infrared signal by mixing it with a strong visible signal, resulting in a viewable output that is easier to detect than the original infrared signal. A "photonic bandgap" fiber can confine light in both a lower index core and a hollow air core by trapping light in a photonic bandgap generated by the microfabricated coating. Bandgap fibers with cores that are hollow have the potential to overcome material limitations, such as creating fibers that control light at wavelengths where see-through materials are not around the corner. Another privilege of a hollow core is that materials can be fluidically introduced into it, for example, a gaseous component that needs to be analyzed for the presence of a substance. PCF can also be upgraded by coating the holes with sol-gels of the same kind or dissimilar index materials to improve its transmittance of light.

2.3.1 The Bandgap Effect

It is a different type of optical fiber with properties that differ from M-TIR guiding optical fibers. Photonic bandgaps are created by the strategic micro-structured arrangement in the cladding region of PBG fibers. Light waves of a certain wavelength range cannot pass through the fibers here. The core regions of PBG fibers are formed by creating a defect in the fiber's structure, which creates a region where light can easily propagate. Because the defect creates a low index-guiding core, light can only pass through it easily. We can't expect this kind of advantage from traditional fibers, and the photonic bandgap fibers' low index-guiding characteristics open up a lot of possibilities. Materials with a recurrent dielectric property, such as photonic crystals (PhCs) or photonic band-gap (PBGs), can avert the light of specific frequencies or wavelengths from advancing in any number of polarization directions within the materials [34]. Photonic band-gap structures can be presented in one, two, and three dimensions. PBGs in one dimension are created through alternating layers with different refractive index values. Chemical vapour deposition (CVD) technology, molecular beam epitaxy, metallo-organic CVDs, and holographic exposure of ultraviolet (UV) beams to photosensitive materials are all examples of fabrication methods.

2.3.2 Modified Total Internal Reflection

By making the refractive index of the material of the core more than the effective refractive index of the material in the cladding, the initial condition is fulfilled. After that, a two-dimensional photonic crystal can be employed. The photonic crystal fiber (PCF) is an example of this type of structure, which is made of a silica solid core surrounded by a cladding with a triangle-shaped lattice of air holes. These aforementioned fibers, also known as index guiding PCFs, guide light through modified TIR, another type of total internal reflection. The core of a solid core PCF is made of pure silica, while the cladding is a photonic crystal with a large number of air holes that lowers the refractive index of the core [35]. The cladding's modified refractive index is less than that of the core, allowing light to travel via modified TIR. PCF cladding is made up of air holes.

The basic mode, which adjusts in the silica core with a single lobe of diameter between zeros slightly equal to or greater than 2, is the "grain of rice" that cannot break out through the wire mesh. Higher-order modes, on the other hand, have smaller lobe dimensions and can, therefore, slide between the gaps. Higher-order modes become captivated, or the air filling fraction of the photonic crystal cladding increases. As a result, a well-designed fiber cross-section ensures that the fundamental mode is led through only. [36].

2.3.3 High Index Guiding Fibers

In the case of optical fibers, M-TIR stands for total internal reflection. They rely on a high-index core, which is usually made of pure silica, and a micro-structured surround that provides a low refractive index. Photonic crystal fibers are very different from conventional optical fibers because this region of cladding is highly wavelength dependent, which is not the same as pure silica. Because the refractive index is strongly correlated with wavelength, we can design infinite single-mode fibers that only support a single mode regardless of wavelength. Furthermore, we can easily manipulate the fibers' dispersion properties, allowing us to design optical fibers with an irregular dispersion characteristic at visible wavelengths.

It is possible to create a very coherent super-continuum generation using photonic crystal fiber technology because of the combination of small cores and phase-matching conditions that are similar to available sources. It is now possible to create optical fibers with large mode-field diameters while controlling the refractive-index profile, allowing for better fiber guidance and amplification.

2.4 Fabrication of PCF

PCFs are made in a variety of ways, but the most common involves creating a macroscopic meter length preform with the desired transverse crystal lattice pattern and drawing it into microscopic scale fibers while maintaining the desired cross-sectional design. Stack-and-draw, extrusion [37], sol-gel casting [38], injection molding, and drilling [21] are some examples of PCF fabrication methods. The most common method is the Knight et al. [21] stack-and-draw technique, which is relatively fast, clean, low-cost, and flexible. **Fig. 2.3** depicts the stack-and-draw method. This

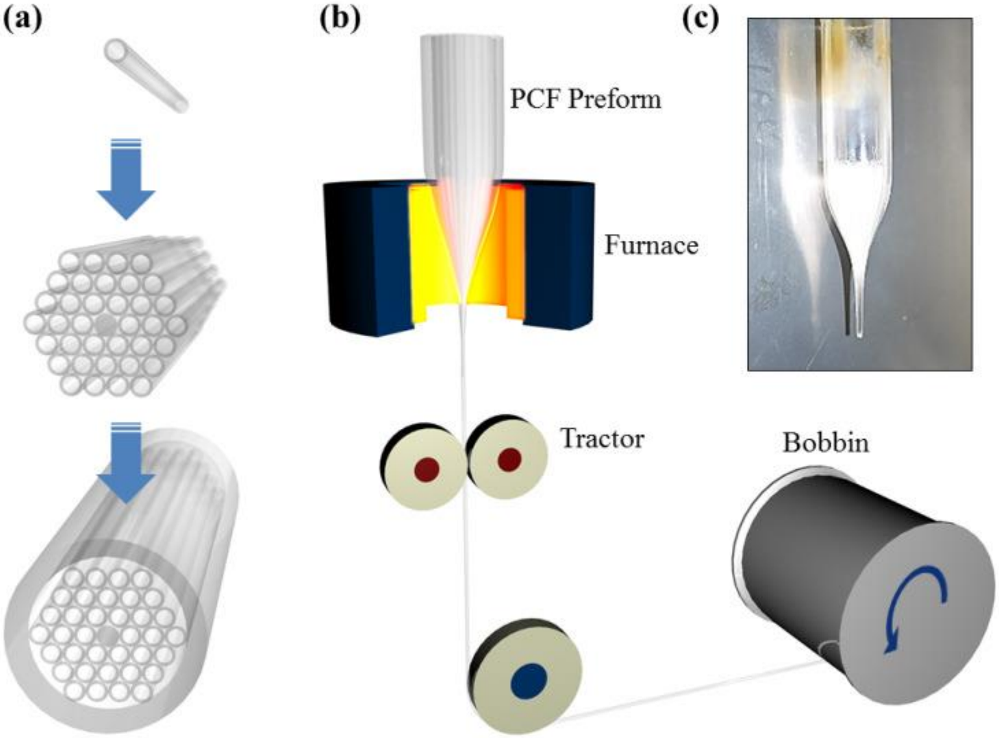

fig. 2.3 *Schematic of stack and draw method (a) Stacking of PCF preform (b) Drawing process of the fiber (c) PCF preform preparation*

specific inner wall over outer wall diameter ratio (ID/OD) determined in design based on PCF hole diameter, d, over lattice spacing, d/. Following that, custom-made jigs are used to arrange the fabricated capillaries into a triangular lattice. Following that, the assembled PCF preform is pulled into fiber using fiber drawing facilities by carefully adjusting the feeding rate, tractor speed, and furnace temperature [38].

2.4.1 Capillaries Fabrication

Capillaries are the fundamental components of a PCF preform made by stacking. Capillary quality should be prioritized to enforce structural asymmetry and uniformity of the lab produced PCF while also reducing cracking tendency and attenuation. Capillaries are made from upper grade silica preform tubes that have been drawn to a nominal outer radius of 0.5~1 mm. If the capillary size is less than 1 mm, it will be hard to keep each capillary in its proper position during the stacking process. Larger capillaries result in fewer rings of air gaps, which alters the PCF guiding property. The feeding rate of the preform and tractor drawing velocity is regulated in accordance with the simplified mass conservation law to control capillary size:

$$A_f v_f = A_d v_d \tag{1}$$

where A_f, A_d are the cross-sectional area of the preform and capillary respectively, v_d is drawing speed and v_f is feeding speed. The furnace's temperature is kept at around 2100°C which is the temperature where silica softens and melts. Higher temperatures increase the surface tension of silica, lowering the ID/OD ratio, and the procedure no longer follows the simplified law. The use of an automatic feedback system ensures capillary size uniformity. In order to produce a well-ordered PCF preform, accurate control of capillary dimension and uniformity is required.

2.4.2 Stacking

Forming the periodic cladding of PCF requires proper stacking. Cleaning and cutting of fabricated capillaries into 30 cm short pieces Capillary contamination increases PCF scattering loss and reduces mechanical strength, so cleaning them before stacking is critical. The dirt deposit within the PCF preform will ignite at a high temperature and spread into the glass matrix, causing further losses and daintiness. Isopropyl alcohol or similar cleaning agents are used to clean the capillary surface, while an ultrasonic bath is used to clean the capillary inner wall. To produce pressure that is high inside the capillaries during fiber drawing, one ending of the capillaries is closed. A high-temperature Butanol-fuel hand torch can be used effectively to prevent PCF holes from breaking down. Capillaries are stacked into a triangle-shaped lattice arrangement using custom-made hexagonal metal parts as guides. Capillaries are chopped into small lengths for simple handling and to prevent the freely flowing lattice from being disrupted by lengthy capillaries bending. Stacking is finished with all sealed ends facing the same way [39]. In a suitable jacketing tube, stacked hexagonal capillaries are inserted, and voids on six hexagonal sides are loaded with rods of various sizes. The core of PCF is formed by replacing the center capillary with a rod of a similar size as the other capillaries. Finally, a metal stop is connected to the end of the PCF preform where the capillaries end is exposed to prevent capillaries from collapsing. If the method described below is used for drawing, the final step is required. [40].

2.4.3 Drawing of PCF

A glass handle should be connected to the PCF preform before drawing. We need to use a newly found process to join two silica preforms leveraging the fiber drawing tower's furnace. Two preforms must be moderately in contact with each other at the heating region of the furnace, with the lower preform rigidly held in place. By looking down from the top, the upper preform is aligned with the lower preform, while the upper preform is moved by a motorized chuck. The temperature of the furnace is then rapidly increased to the silica melting point of 2100°C. When the temperature reaches 2100°C, it is instantly lowered to 1600°C or less.

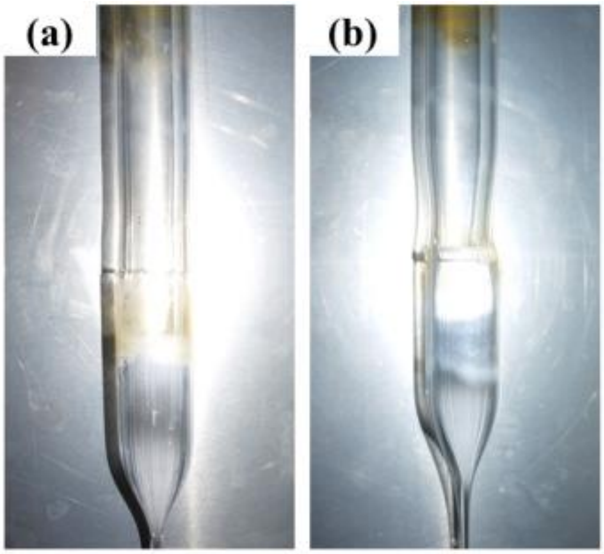

fig. 2.4 *PCF preform connected with silica tube (a) Successful preform connection (b) Waist deformation*

As shown in **fig. 2.4**, this procedure will ameliorate two performers together without causing waist deformation. The PCF preform is then heated and cooled afterward. Later, it is polished in a furnace at a high temperature (1700°C) with a quick recurring perpendicular motion to moderately combine the jacketing tube with the capillaries inside. Only fiber drawing facilities are required for the aforementioned procedure. This further obviates the need for a preform lathe equipped with a high-temperature hydrogen-oxygen-fuel burner.

PCF is drawn in two steps: caning and fiber pulling. PCF preform is drawn to 1- 2mm canes in the first stage. During the process, the drawing speed is gradually increased to achieve the desired cane length. The furnace's temperature is set between 1900-2000℃. Temperatures above 2000°C will cause air-holes to collapse, while temperatures below 1900°C may cause random cracks. Applying vacuum inside the preform closes interstitial holes, the cross-sectional surface of cane samples is examined under a microscope on a regular basis to ensure that the correct structure pattern is formed. The second stage involves sealing one end of the PCF cane with a hand torch and inserting it into a suitable silica cladding tube. The cladding tube chosen is determined by the microstructure's final scaling. Using a cladding tube with a higher inner wall over outer wall diameter ratio (ID/OD) ratio will project in smaller hole and pitch sizes, and vice versa. The PCF cane must be heated in the furnace prior to the second stage drawing at 1600°C for a few quick passes, with the goal of creating a uniform temperature environment in all air-holes. In this way, the fabricated PCF has a uniform microstructure along the fiber. Drawing cane to fiber is done in the same way as the first stage, with careful control of drawing speed, temperature, and pressure.

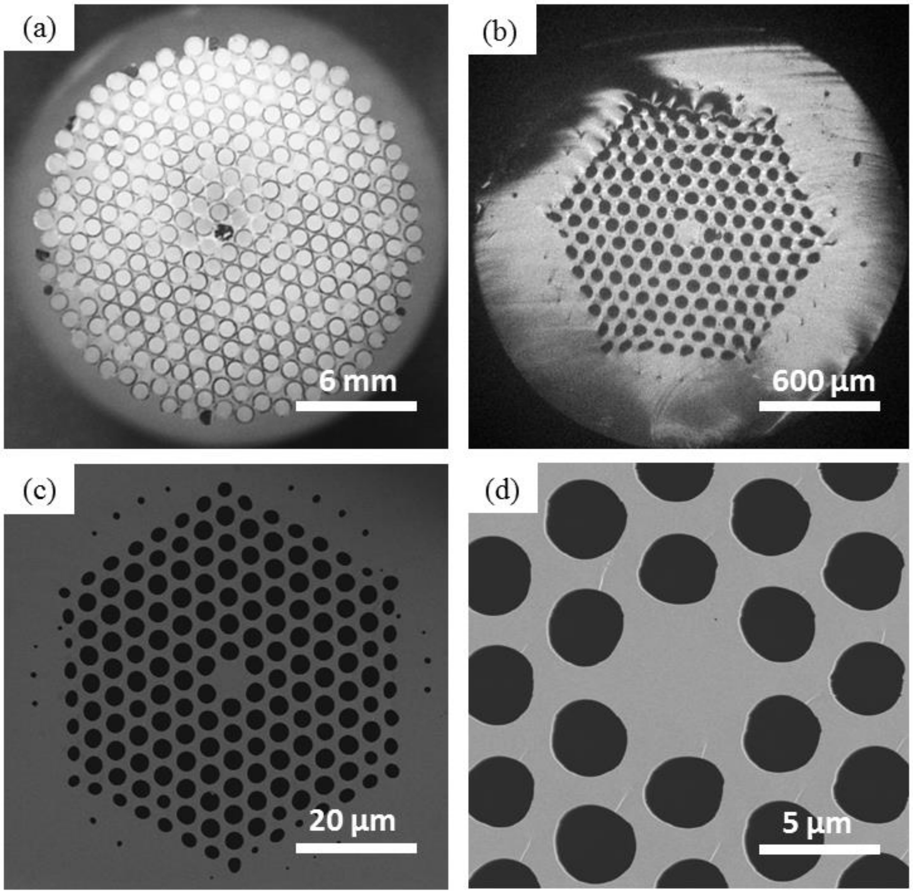

fig. 2.5 *Cross-section of PCF at different stages (a) PCF preform (b) PCF Cane (c) PCF of 125 µm diameter (d) Microstructure around PCF core*

The cladding tube is sucked inside, causing the space between the PCF cane and the cladding tube to narrow in the furnace due to air pressure. Unless the holes are planned, the temperature of the furnace is gradually incremented with the objective to minimize interstitial holes. This is a very important step in this process and therefore requires to be done very carefully. When the process is stable, dip-coating and UV curing equipment are used to coat the fabricated PCF, and the coated PCF is then wound into a large spool utilizing a Capstan winder. **fig. 2.5** shows a sample cross-sectional view of PCF from preform to fiber. Different microscopic stages of a typical PCF fabrication process can be observed in the figure.

Chapter 3

Surface Plasmon Resonance

3.1 Introduction

Surface Plasmon Resonance (SPR) is a detection method that refers to an optical phenomenon which happens when a photon of incident light falls on a metal surface at a particular angle. SPR based PCF sensors are playing vital role in optical sensing. Usually for the label free detection, lightweight and flexible detection capability, it is popular now-a-days in the biomolecular sectors.

Surface plasmon polariton refers to a non-radiative electromagnetic surface wave that promulgates parallel to the negative permittivity/dielectric metal interface. Because the wave is situated on the conductor's boundary with the external medium (vacuum, air, water, etc), any alternation in this boundary, like molecule adsorption on the conducting surface, will cause oscillations [41].

Various models can be used to explain the existence and properties of surface plasmon polaritons (quantum theory, Drude model, etc.). The clearest way to address the problem is to treat each material as a homogeneous continuum with a frequency-dependent relative permittivity between the external layer and the surface. The complex permittivity is the quantity referred to as the "dielectric function" of a material. In order for the terms that characterize the electronic surface plasmon to exist, the real component of the conductor's dielectric constant must be below zero and its magnitude must be greater than that of the dielectric. These are some of the prerequisites for the plasmons to form. For air/metal and water/metal interfaces, in the infrared-visible wavelength region, this condition is fulfilled[42], [43].

3.2 Working Principle

Electron bombardment or incident light beams can be used to resonantly excite surface plasmon polaritons. Typically, infrared and visible light is used. The coming beam must have the same momentum as the plasmon [44]. This is possible with p-polarized light by projecting the light through a block of transparent silica media to increase the wavenumber and attain resonance at a specific angle and wavelength. Electronic surface plasmons cannot be excited by S-polarized light where the polarization takes place perpendicular to the incidence plane. The dispersion relation for electronic and magnetic surface plasmons is as follows:

$$k(\omega) = \frac{\omega}{c}\sqrt{\frac{\varepsilon_1 \varepsilon_2 \mu_2 \mu_1}{\varepsilon_1 \mu_1 + \varepsilon_2 \mu_2}} \tag{2}$$

Where, ε is the relative permittivity, *k(ω)* numerizes the wave vector, and μ is the relative permeability of the materials, while ω is the angular frequency and *c* is a medium-specific constant known as the speed of light. Here, vacuum is considered. Silver, Copper, and Gold are common metals that support surface plasmons, but titanium and chromium have also been tested in many works of literature [41].

There are two well-known configurations for using light to trigger SP waves. The light illuminates the wall of a glass block, in the Otto configuration, and is completely reflected internally. A thin metal film made of any plasmonic material is placed adequate proximity to the prism boundary for an evanescent field to interact with the waves of plasma on the surface and thus the plasmons are excited. On the crystal block, the metal film evaporates in the Kretschmann configuration (also known as Kretschmann–Raether configuration). An evanescent wave flows through the metal coating when the light shines on the glass block once again. The plasmons are excited on the film's external side. In most practical applications, this configuration is used.

When SPR occurs, the frequency of the incident light and excited electrons on metal surface is similar. An incident light projects on a metal surface at a specific angle. The incident light is monochromatic polarized light coming from a laser. The incident light propagates through the metal layer. The electrons near the metal surface get excited by the incident photon energy and thus an evanescent field is generated within a detection area (usually <500 nm) on the metal surface. The excited electrons are called surface plasmons and SPW (Surface Plasmon Wave) is radiated. The optical detector analyzes the reflected beam. The density of the molecules affects the particular Resonance Angle (RA) [45]. So, when the analyte molecule binds with the surface ligands, the refractive index near the surface shifts. This causes a reduction in the intensity of the reflected light which appears dark in the detector. Also, the incident RA angle also changes. Thus, unknown analyte is detected through the monitoring of RI change.

Usually Glass is used as dielectric material and Gold is used as the metal. A sensorgram is a plot of response against time. It shows the interaction progress. From the sensorgram the dynamics, binding affinity and many more information are extracted.

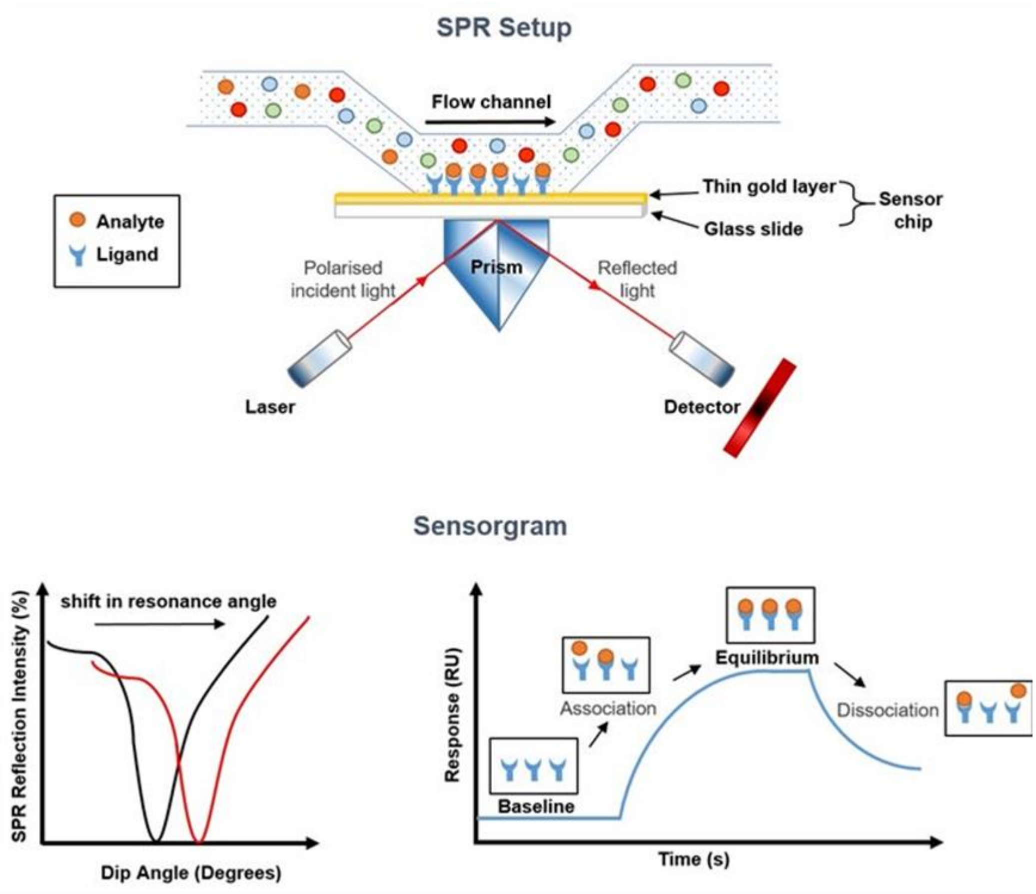

fig. 3.1 *The conventional SPR setup with working principle*

3.3 Literature Analysis

There are some terms in SPR like Surface Plasmon Wave (SPW), Surface Plasmon Polariton (SPP), Evanescent Field etc. These will be discussed here.

3.3.1 Surface Plasmon Wave

When the incident light falls at a particular angle, some energy is lost because it propagates through the cladding to the plasmonic material. It couples to the plasmonic material which creates resonant oscillation of the electrons in the analyte-metal surface. Then SPW is generated in the analyte-metal surface. It is a transverse wave which is normal to the surface. Metallic lines, strips, and tubes are commonly used in RF transmission lines and microwave waveguides. Metal is viewed as a perfect conductor in the low-frequency region. Metal can no longer be viewed as a flawless conductor in the UV and visible regions due to its common electron excitation, known as the plasmon. It can, however, be used to make metal-dielectric waveguides and low-loss metal waveguides. The electromagnetic field in these two structures takes the configuration of an evanescent wave. Noble metals, like gold, silver, aluminum, etc., on the other hand, have a greater real part than imaginary part in their complex permittivity. This relation can be understood from the below equation:

$$\varepsilon = \varepsilon_r + i\varepsilon_i, \varepsilon_r < 0, |\varepsilon_r| \gg \varepsilon_i \tag{3}$$

Due to this optical characteristic, the surface plasmon wave (SPW) can propagate along the metal-dielectric interface, and the long-range SPW can be excited within a very thin metallic slab. These two surface waves show how they differ from a traditional waveguide. The huge range of the effective RI and the field enhancement effect are two examples of unique characteristics that can be valid. SPW propagation not only enriches the traditional waveguide optics research field, but also has a broad range of implementations in fields like molecular biology, integrated optics, nonlinear optics, and so on [46].

3.3.2 Surface Plasmon Polariton

Surface plasmon polaritons (SPP) are a type of electromagnetic waves that propagate in the visible or infrared ranges alongside a metal-air or metal-dielectric interface. The title "surface plasmon polariton" describes a wave that includes both charge motion in electromagnetic waves and metal in the air or dielectric [41]. They're a kind of surface wave that travels along with the interface in the similar way that light travels through an optical fiber. SPPs have a smaller wavelength than light ray at the same frequency in vacuum medium. [47]. As a result, SPPs have more momentum and local field intensity. They have subwavelength confinement vertically positioned to the interface. An SPP will advance alongside the interface until it loses energy due to metal absorption or scattering in other directions (such as into free space). The electrons oscillations are electromagnetic oscillations and until the energy is free in metal concentrations or in some other way, the SPP keeps expanding [48], [49]. A typical schematic has been shown in figure 3.2.

Both photons and electrons can be used to excite SPPs. Electron excitation is achieved through firing electrons into a metal's body [50]. Energy is transferred into the bulk plasma as electrons scatter. When a component of the scattering vector is parallel to the surface, a surface plasmon polariton is generated[44]. A photon is required to have the same momentum and frequency as an SPP to excite it. However, a free-space photon has less momentum than an SPP because their dispersion relations are different for a given frequency. A free-space photon from the air is unable to couple candidly to an SPP due to this momentum mismatch. A smooth metal surface SPP cannot emit energy into the dielectric as a free-space photon for the same reason (if the dielectric is uniform). During total internal reflection, there is no transmission and this lacking is analogous to this incompatibility [51]. Using a coupling medium that matches the photon and SPP wave vectors, photons can be transformed into SPPs, such as a prism or grating. In the Kretschmann configuration, a prism is placed against a thin metal film, while in the case of the Otto configuration, it is placed very near to a metal surface as displayed in **fig. 3.3**(a), (b). By raising the parallel wave vector component by a factor proportional to the grating time, the wave vectors are matched. While this procedure is less commonly used, it is imperative to the theoretical analysis of surface roughness. Furthermore, simple isolated surface defects on an otherwise planar surface, such as a groove, a slit, or a corrugation, create a mechanism for free space radiation and SPs to interchange energy. Thus, coupling is occured.

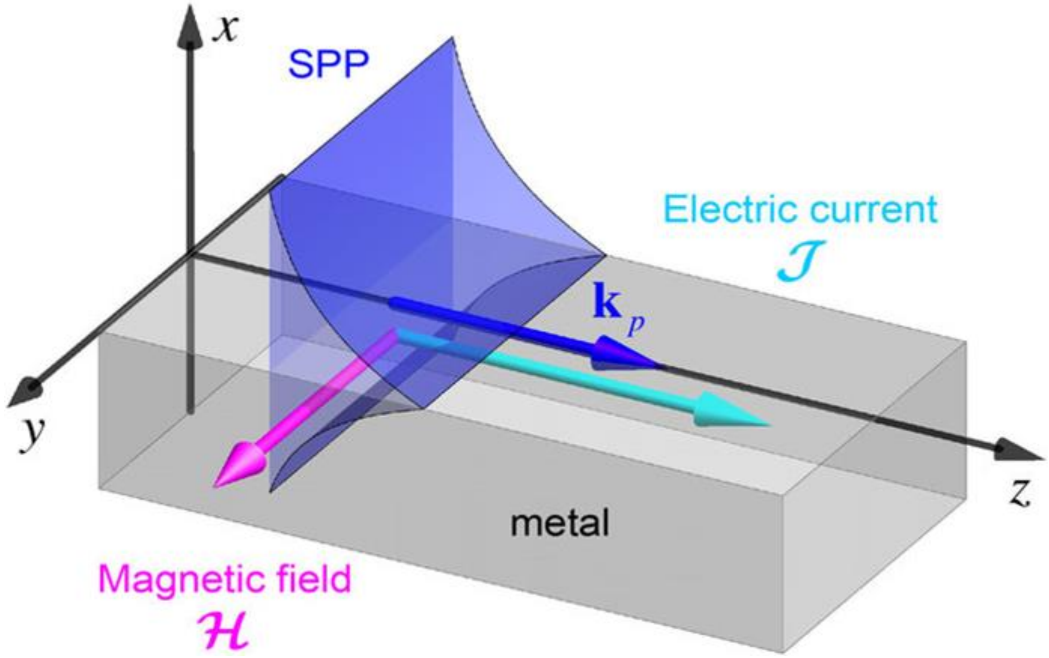

fig. 3.2 *Schematic of Surface Plasmon Polariton*

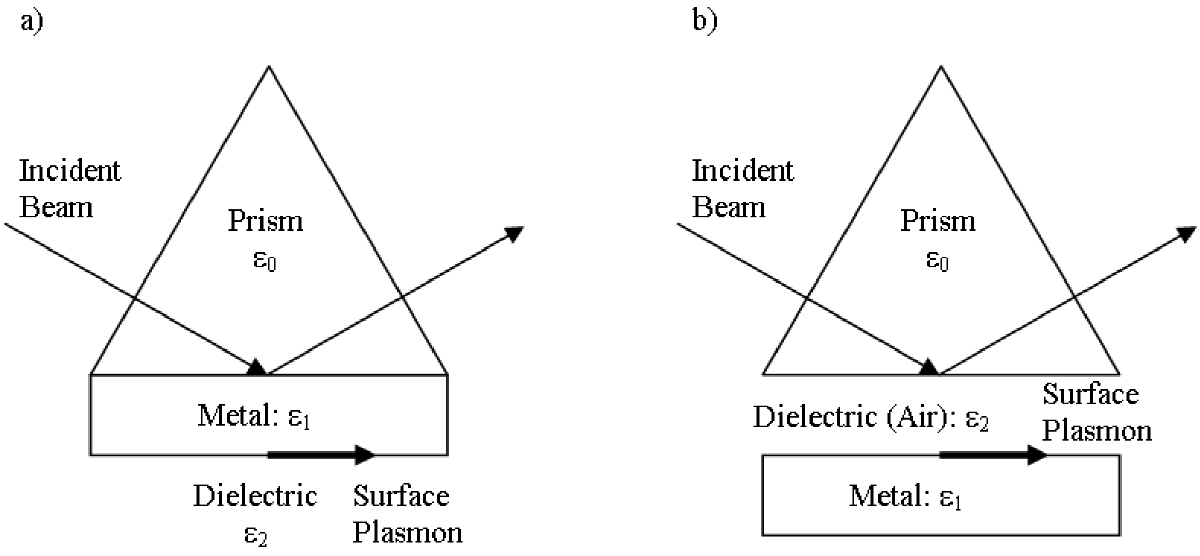

fig. 3.3 *(a) Kretschmann and (b) Otto configuration of an Attenuated Total Reflection setup for coupling surface plasmons.*

3.3.3 Evanescent Field

An evanescent field, also known as an evanescent wave, is an oscillating electric and/or magnetic field that does not promulgate as an EM wave but has its energy spatially centered near the origin [52]. Even when an advancing electromagnetic wave is created (for example, by an antenna), the element of the electric or magnetic field that cannot be ascribed to the propagating wave perceived at a gap of many wavelengths can be identified as an evanescent wave. The reflected light has an angle near the critical angle but not the critical angle because some light energy is lost in the cladding of the dielectric from the core and in the metal surface some light is absorbed by the electrons. The evanescent field is created within the surface area and exponentially decays [53]. A typical formation of an evanescent field has been shown in **fig. 3.4**.

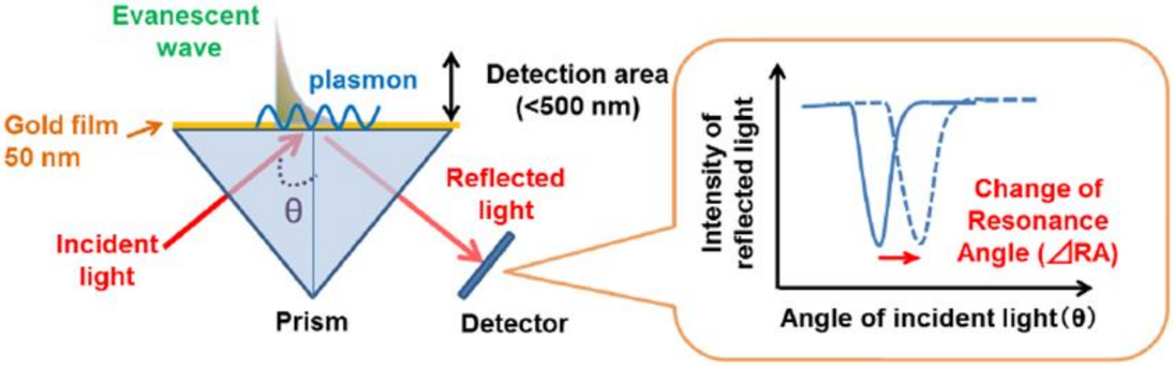

fig. 3.4 *Evanescent Field*

3.4 SPR Advantages

SPR technology is easily reliable and accessible. has been contributing for two decades in various areas of Optics, Microbiology, Biomolecular science, Environmental science and so on. There are few advantages of this type of technology.

- **Real time and remote monitoring** - SPR technology expands the analysis on how different bio-molecules interact with each other, how much energy is used etc. It has made this so much easier to observe all the details information of bio-molecular binding in real time like affinity, kinetics and so on.
- **Label free detection** - It enables no labelling method of measuring the bio-molecular interaction. It is definitely one of the important reasons to prefer SPR over any other technology.
- **High accuracy** - The results occurred are highly accurate. Many experts still depend on the traditional expensive methods in bio-sensing. But SPR has a remarkable accuracy too.
- **Affordable** - It requires small amounts of precious samples. So, it is less expensive, saving the money. Also, there is no expensive optical instruments.
- **Reusable** - The sensor chips are reusable. Regeneration buffer can be used to disrupt the interaction between the analyte and ligand. So, it has a huge economical advantage.

3.5 SPR Applications

Several spectroscopic quantification such as second-harmonic generation, fluorescence, Raman scattering, etc. have been improved by using surface plasmons. SPR reflectivity measurements may be used to identify molecule adsorption, such as polymers, DNA, and proteins, in their most basic form. The angle of minimal reflection is commonly measured in technical terms (angle of maximum absorption). During slim film adsorption, this angle changes by 0.1°. In other cases, the absorption wavelength changes are monitored[54]. The detection mechanism is based on the fact that adsorbing molecules change the local index of refraction, changing the surface plasmon waves' resonance conditions [55]. Surface plasmon resonance imaging (SPRI) can be used using this technology if the surface is decorated with a repeated design with different biopolymers and reasonable optics and imaging sensors are used. This approach, which is comparable to Brewster angle microscopy, produces high contrast pictures based on the number of molecules adsorbed. The profound colors of sols or suspensions containing nanoparticles can be attributed to localized surface plasmon oscillations. Noble metal nanoparticles or nanowires have strong UV-visible light absorption bands that are absent from the bulk metal. This exceptional absorption increase has been utilized by depositing metal nanoparticles on the cell surface to improve light absorption in photovoltaic cells[56]. When light is polarized perpendicularly to the nanowire, the energy (color) of this absorption changes. Modification in the local index of refraction caused by adsorption to nanoparticles can also be used to discover the existence of biopolymers like DNA or proteins [57]. Dual-polarization interferometry, plasmon waveguide resonance, QCM, extraordinary optical transmission, etc. are all complementary techniques. SPR technology also unveiled new opportunities in many sectors like:

- **Medical Diagnostics -** Diagnosis of any virus, presence of virus in blood samples, glucose monitoring, etc. has become easier for SPR technology.
- **Organic Chemical Sensing -** The binding interaction between different protein molecules can be measured and various informations like specificity, affinity, kinetics, etc. can be extracted.

- **Telemedicine-** Telemedicine needs real time, remote monitoring service. So SPR technology is used here.
- **Environmental Sensing** - The temperature, magnetic field, and other environmental factors can be detected through SPR technology.

Bioimaging- If the surface is decorated with biopolymers, then to acquire the structural overview of the living object the SPR technology is used too.

Chapter 4

Photonic Crystal Fibers based on SPR

4.1 Introduction

In earlier the kretschmann configuration paved a way for prism based SPR sensors. A gold film and sample solution with a prism to initiate Total Internal Reflection was the configuration of prism-based sensors. The prism was used so that the electrons in the coated metal gets excited and produce Surface Plasmon Wave. But this type of configuration was not feasible for remote sensing. The unknown analyte layer had to be used outside [10] and they were not size friendly. Also, in case of curved surfaces it would use complexity [58].

Then finally in 1996, PCF fibers were introduced. Because of its capability to confine light in the hollow core which is not possible in conventional optical fibers, the SPR based PCF sensors opened new opportunities in optical fiber communication. Due to their high sensitivity, structural flexibility, smaller size, label free detection technique, real and remote monitoring technique they were suitable for unknown analyte sensing and other applications in bio-sensing, medical diagnosis, microbiology and medicine, environmental monitoring and so on. There are Propagation Surface Plasmon Resonance and Localized Surface Plasmon Resonance. The PSPR happens at the interface of dielectric and metal surface while localized happens at the rugged surface of nanostructured metals [59], [60] .

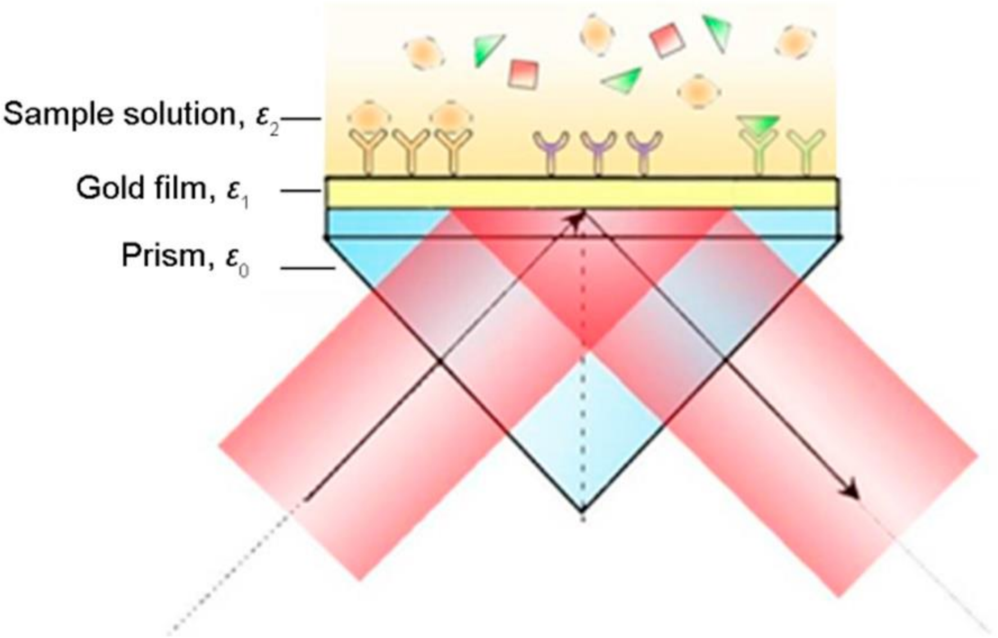

fig. 4.1 *Kretschmann Configuration of Prism based SPR sensor*

.

4.2 Types of Sensing

There are two types of approaches in case of sensing- internal and external sensing. In internal sensing the analyte is in the air holes. The air holes form analyte channel. In external sensing the analyte is place outside the metal at the outside surface of PCF [61].

In the internal Sensing the metal is coated in the air holes and the air holes contain the analytes. But these types of sensors had complications in case of structure and fabrication. The filling out of air holes, coating the metal in the air holes and maintaining uniform radius is difficult in practical aspect. Below in **fig. 4.2.1** is a PCF sensor introduced with internal sensing [62].

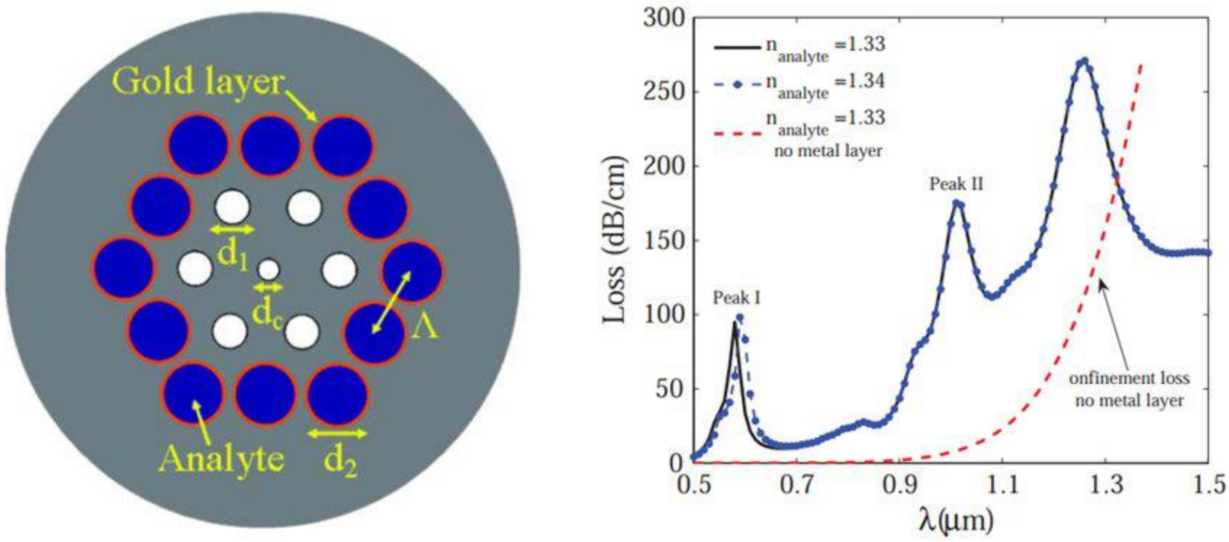

(a) (b)

fig. 4.2.1 *(a) Internal Sensing structure (b) Loss curve*

In the external Sensing, the metal is coated and then the analyte layer is present. So, it has an advantage over internal sensing that the Sensor can be reused. Also, there are lesser complexity in structures. Below in **fig 4.2.2** is a PCF sensor introduced with external sensing [63].

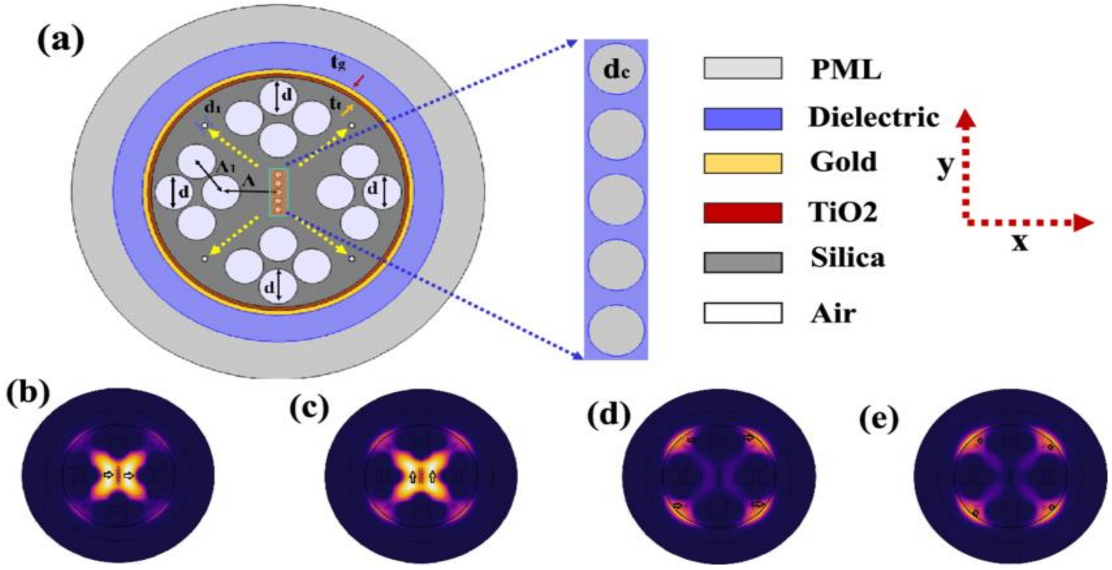

fig. 4.2.2 *(a) External Sensing Structure, (b)-(e) Core and SPP modes for both pol*

4.3 Types of PCF Sensor Structures

There are various structures of PCF based on SPR sensors. Here are some structures used most commonly.

4.3.1 D-Shaped Structure

When the fabrication of internal sensing was difficult and it was not reusable, the D-shaped sensors were proposed. The D-shaped fiber is easier to fabricate and on flat surface has to be coated with plasmonic material. In **Fig 4.3.1.1**, the basic structure of a D-shaped structure is given [64].

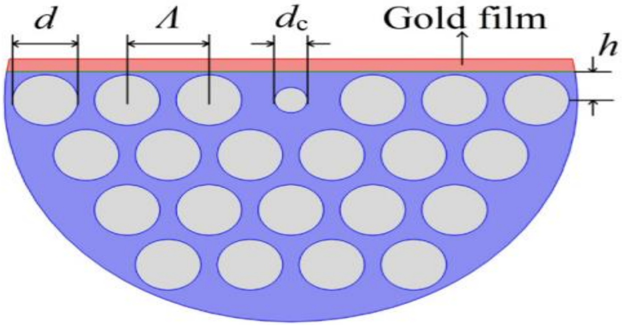

fig. 4.3.1.1 *D shaped structure with hollow core*

A MCCF Sensor was also proposed to ease the way of fabrication in 2016. Although it had an easy sensing approach, it had a maximum sensitivity of 820 RIU^{-1} with a low sensing range. For increasing more sensitivity and resolution and other parameters later on more improved and technically convenient D-shaped structures were proposed. In February, 2018 Xin Chen proposed a D shaped sensor with a open ring channel. The channel was coated with plasmonic material Gold. The maximum wavelength sensitivity was achieved 11055 nmRIU^{-1} [65]. In August 2018,with open ring coated metal structure, Emranul Haque proposed a sensor with more wavelength sensitivity of 20000 nmRIU^{-1}[66]. Later on, in January 2021, Emranul Haque proposed another sensor with wavelength sensitivity of 216000 nmRIU^{-1}.The D-shaped structures are easy to fabricate which makes them the most common structure [67].

Table 4.3.1 *Comparison of D-shaped structure*

Ref	Wavelength sensitivity (nmRIU^{-1})	Resolution (RIU)	Sensing range
[65]	11055	9.5x10^{-6}	1.20-1.29
[66]	20000	5x10^{-6}	1.18-1.36
[67]	216000	4.63×10^{-7}	1.23-1.42

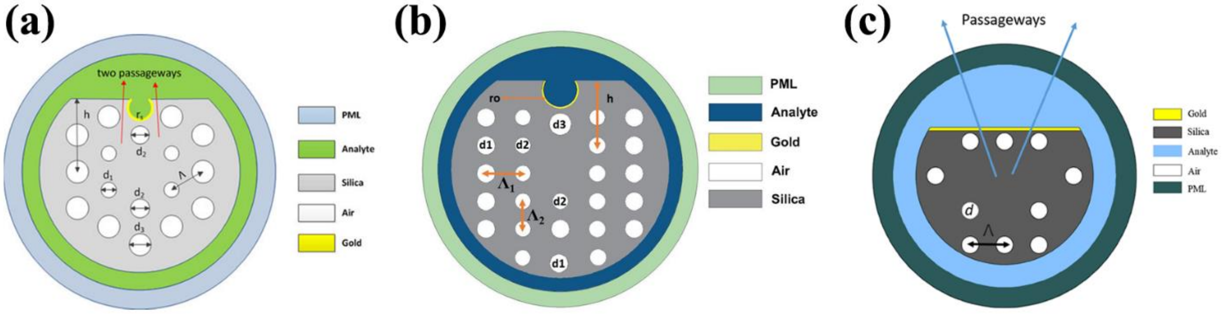

fig. 4.3.1.2 *(a)[65] (b)[66] (c)[67]*

4.3.2 Hexagonal Lattice Structure

In Hexagonal Lattice Structures, to increase the relative sensitivity and decrease the confinement loss among the proposed sensors and to have a high birefringence and high non-linearity, different sensors were proposed shown in Fig 4.3.2 and 4.3.2.1 [68], [69].

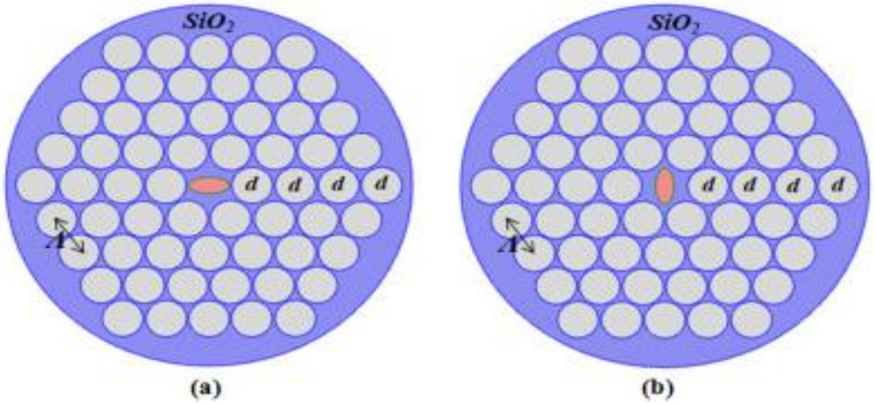

fig. 4.3.2.1 *A hexagonal PCF structure varying the elliptical hole in the core (a) vertically (b)horizontally*

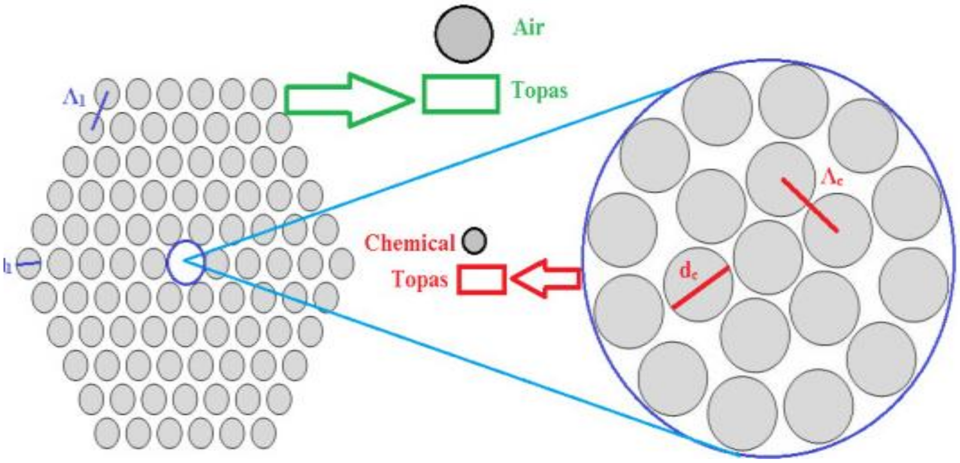

fig. 4.3.2.2 *A hexagonal cladding PCF structure with core in the middle*

In 2016, A.A Rifat proposed a sensor with 3 rings of air hole placed hexagonally. The wavelength and amplitude sensitivities of the sensor were 1000 nm/RIU and 118 RIU-1, respectively[70]. In 2019, S.M Abu proposed a sensor with hexagonal structure, that had good wavelength sensitivity in both polarizations [71]. Later in 2019, Tanvir Ahmed proposed a Dual core structure with more wavelength sensitivity which was also hexagonal structured with a maximum wavelength sensitivity of 16000 nmRIU^{-1}[72].

Table 4.3.2 *Comparison of Hexagonal structures*

Ref	**Wavelength sensitivity (nmRIU^{-1})**	**Resolution (RIU)**	**Sensing range**
[73]	22,983	10^{-6}	133-1.41
[71]	13000	$7.69 \text{x} 10^{-6}$	1.33-1.37
[74]	29500 (x pol) 9500 (y pol)	3.39×10^{-6} 1.05×10^{-5}	1.33-1.43

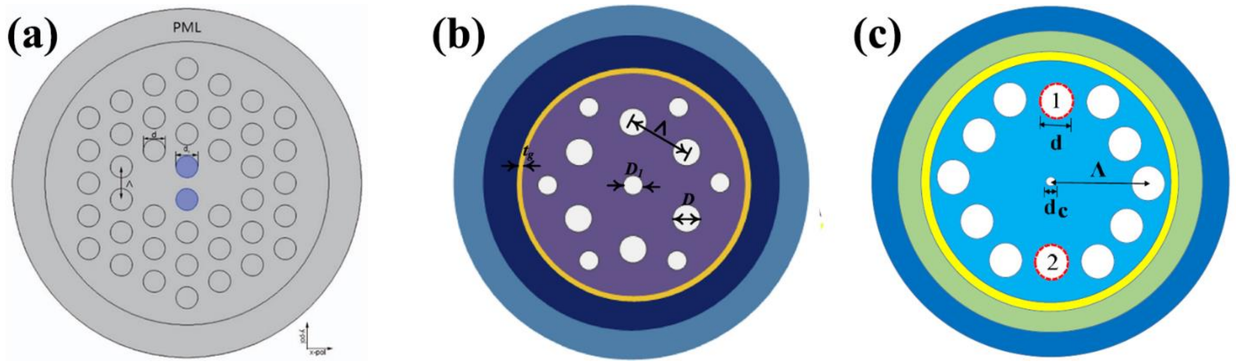

fig. 4.3.2.3 *(a) [73] (b)[71] (c) [74]*

4.3.3 Circular Lattice Structure

There have been many circular structures proposed until now. In 2017, Md. Rabiul Hasan proposed a circular structured showed in Fig 4.3.3,

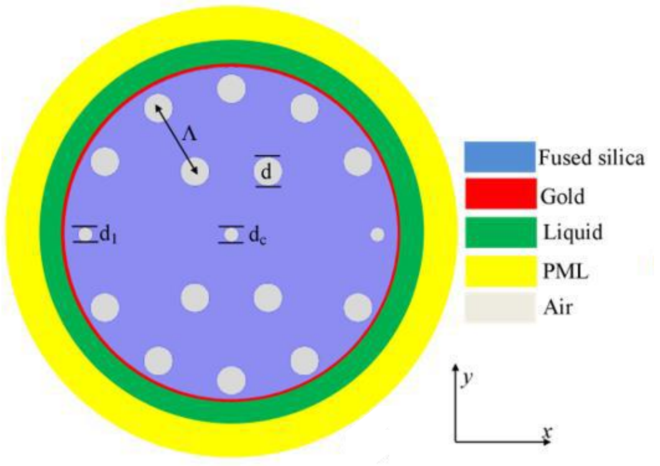

fig. 4.3.3.1 *Circular structured PCF sensor*

The design has two sets of air holes- one smaller and one bigger. The whole structure has a full circle of air holes near the outer cladding boundary. There are 10 big and 2 small air holes. There is also a small air hole at the center. The air holes on x axis are smaller. There are also 4 extra air holes around the center air hole. The highest wavelength sensitivity was 2200 nm/RIU with a sensing range of 1.33-1.36 [75].

In August 2018, Md. Khalek proposed a design with sensitivity of 9000 nm/RIU [76]. In August 2020, A dual core circular structured sensor was proposed and it was examined near the infrared region. Its wavelength sensitivity is 11200nm/RIU [77].

Table 4.3.3 *Comparison of circular lattice structures*

Ref	Wavelength sensitivity (nmRIU^{-1})	Resolution (RIU)	Sensing range
[76]	9000	1.11×10^{-5}	1.34-1.37
[77]	11200	8.92×10^{-6}	1.33-1.44
[78]	12100	8.26×10^{-6}	1.31-1.40

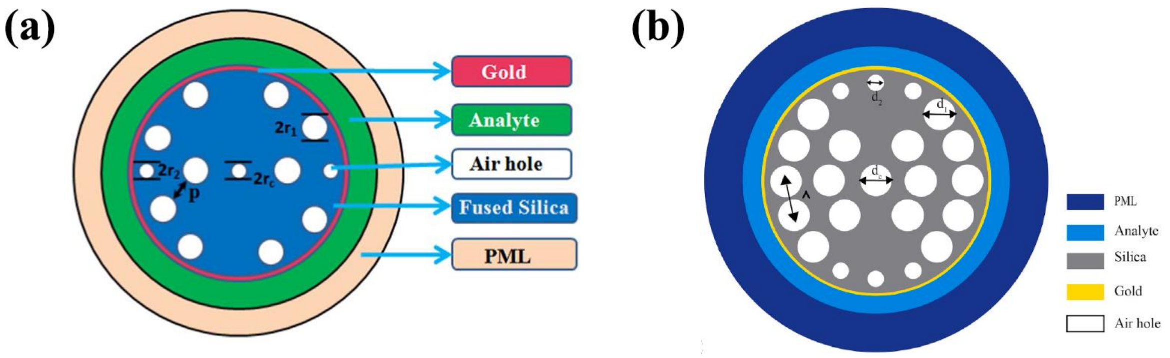

fig. 4.3.3.2 *(a) [76] (b) [76]*

4.3.4 Trigonal Structures

There are many other proposed designs. In 2018, Saiful Islam proposed a gold coated plasmonic sensor that had trigonal clustered structure of air holes in cladding which had a sensitivity of 62000nm/RIU [79]. In February 2022, Md. Rakibul Islam proposed a trigonal clustered sensor which had wavelength sensitivity of 28500 nm/RIU [11].

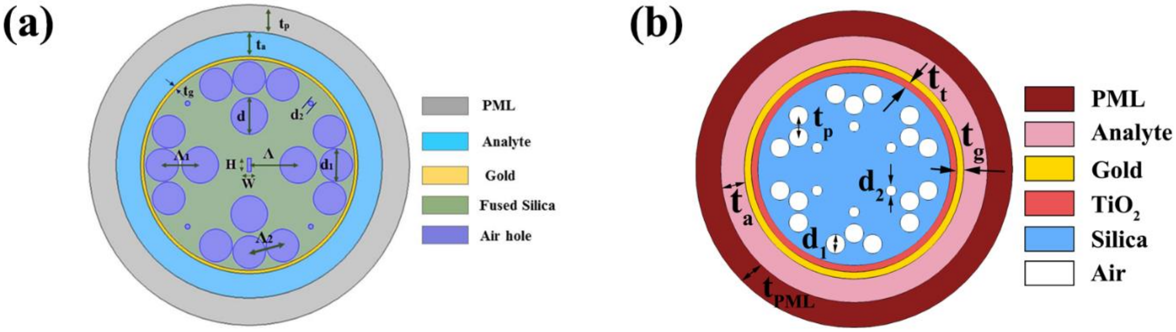

fig.4.3.4 *Trigonal Structured PCF*

4.3.5 Trapezoidal Structures

In 2019 Suoda Chu proposed a unique six folded design to increase the detection accuracy of sensor. The design was D shaped with a trapezoidal shaped channel. It was for infusing the liquid analyte. The low confinement loss and wider wavelength range was achieved due to this unique design. The height of the analyte was altered like 20%, 25% and 50% and the sensor performance changed along with the sensor range. Gold was used as plasmonic material and the highest sensitivity gained was 4400, 6100, 8000, 17000nm/RIU for range of respectively 1.44 to 1.57, 1.41 to 1.51, 1.40 to 1.49 and 1.40 to 1.44 [80].

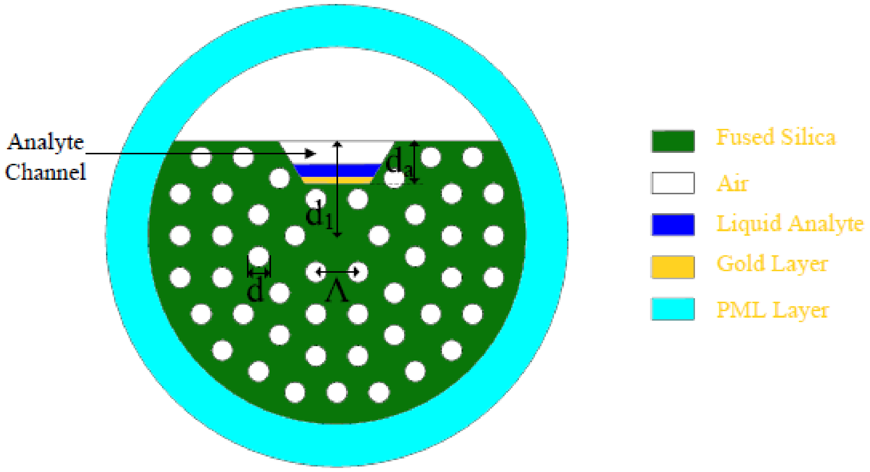

fig. 4.3.5 *Trapezoidal channel-based PCF*

4.3.6 Square Structures

For increasing the resolution and sensitivity of sensor, in 2018, Md. Nazmul Hossain proposed a square latticed sensor. The sensor has two types of air hole with two square layers. There is a tiny air hole at the center and 4 air holes are missing in the square lattice. Gold was coated outside it [81]. The sensitivity and resolution was 6000 nm/RIU and 1.66 × 10^{-5} respectively.

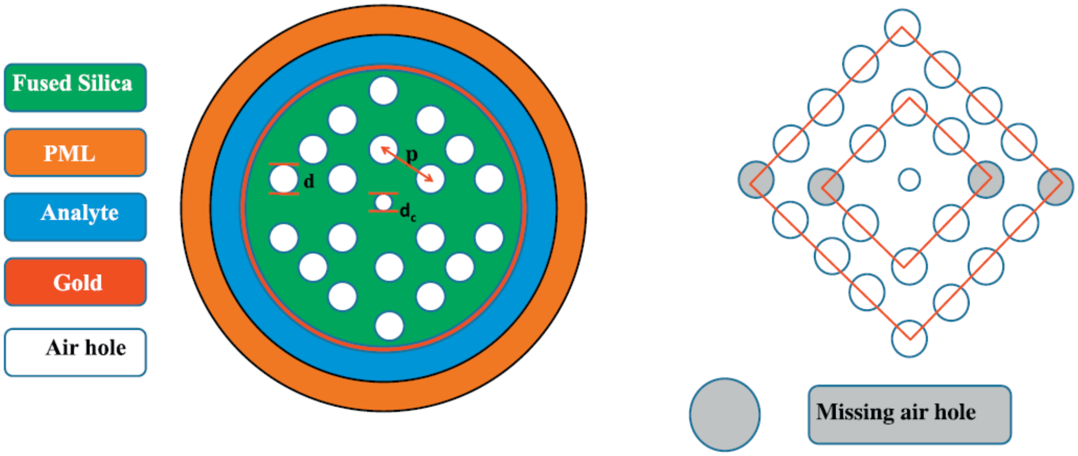

fig. 4.3.6 *Square lattice PCF design*

4.3.7 Spiral Structures

In 2018, Md. Rabiul Hasan proposed a sensor which is spiral structured. There is six arms and three rings. The first two horizontal arms are missing one ring to create asymmetry. This was to create birefringence asymmetry which would increase the coupling between polarized modes and spp modes. So overall the design was created to increase the sensor performance. This sensor showed sensitivity of 4600nm/RIU and 4300nm/RIU in the x and y pol respectively and the sensing range was 1.33-1.38 [82].

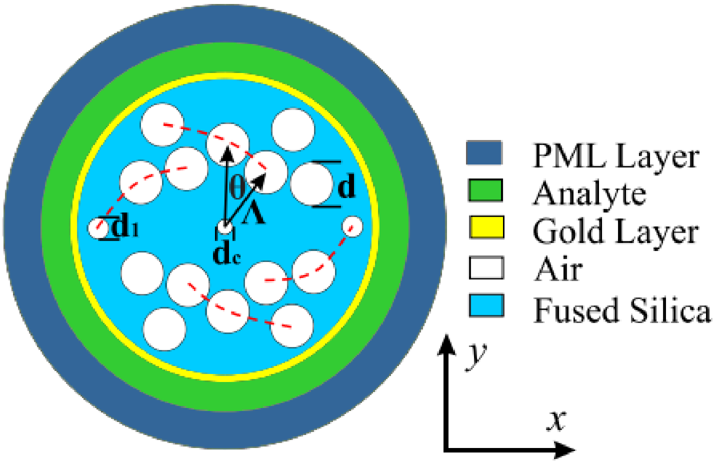

fig. 4.3.7 *Spiral Structured PCF sensor*

4.4 Plasmonic Material on PCF

In PCF, the plasmonic material plays an important role in case of sensitivity, resolution and loss. Materials need to be plasmonic so the energy loss is lesser and coupling is stronger. Many plasmonic material are used such as Gold, Silver, AZO, Copper etc. In **fig 4.4** , the real and imaginary values of the permittivities of the plasmonic materials are given [83].

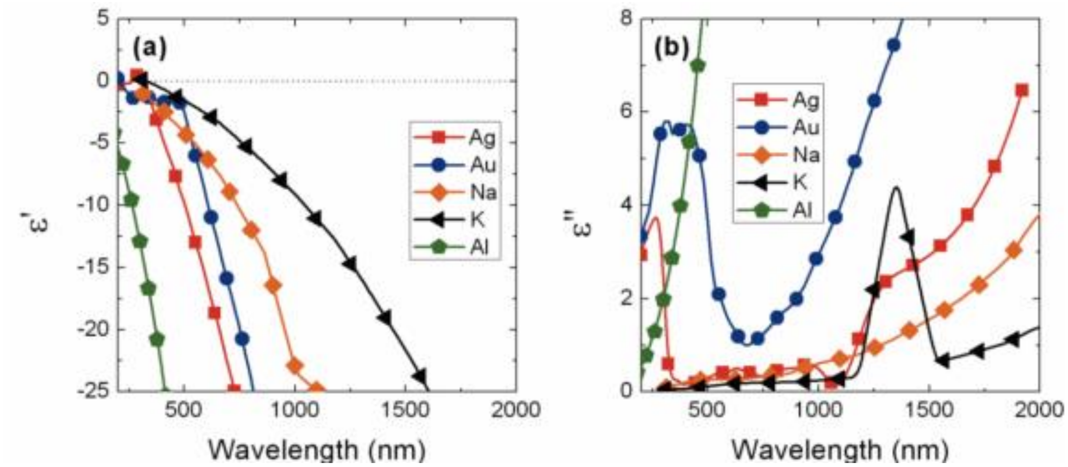

***fig. 4.4** The real and imaginary permittivity of Ag, Au, Al along with K and Na*

4.4.1 Gold

In PCF sensors one of the most commonly used plasmonic material is Gold. Gold is used because of its excellent absorption property in visible and near infrared range [84]. The ohmic losses are much lesser than other materials [18]. Gold is the most common plasmonic material because-

- It is a chemically stable material
- It does not get oxidized in any aqueous environment
- It has a broader peak shift which makes it easier to detect the RI change
- Due to excellent plasmonic property, it gives higher sensitivity.
- It gives sharp resonant peak

4.4.2 Silver

Among the noble metals, Silver has the lowest loss in the visible and infrared spectrum.it gives good results in sensor performances. Silver is used because -

- It has high conductivity
- Less ohmic losses in optical frequencies
- Gives lower damping loss
- Shaper resonance peak

But Silver has chemical instability. It can be oxidized easily and degrades quickly [82], [83].

4.4.3 Copper

After the most conductive material is Copper. Consideing the expense of Gold and Silver copper is suitable in PCF sensors too. It gives good results in case of sensitivity. But the fabrication of PCF with copper is very challenging because it is not chemically stable and forms Copper Oxide very easily[83].

4.4.4 Aluminium

Aluminium has high value of complex permittivity in visible range than Gold, Silver. But in UV and blue region the value of complex permittivity is lower which makes Aluminium better plasmonic material in UV and blue range. In atmospheric environment, Aluminium forms Aluminium oxide making the fabrication process harder. Still in LSPR Aluminium is vastly used to observe optical properties in UV and Blue range [83].

4.4.5 Transparent Confucting Oxides (TCO)

The semiconductors like Zinc oxide can be heavily doped to make conduction film. Due to huge bandgap, they are transparent in visible range. That is why they are called TCO. The low less metals like Gold, Silver, Aluminium gives negative refraction in the NIR regions which is a problem. The high loss materials then provide good tranmittance. That is AZO, GZO, ITO, etc are good for NIR region as plasmonic materials [85].

- Aluminium doped ZnO (AZO) is a good choice for plasmonic material. Though Aluminium gets oxidized but AZO gives good results sometimes better than Gold in case of sensor performances. It gives sharp peaks and works well in the NIR region.
- Gallium doped ZnO (GZO) is also used for plasmonic materials. The GZO has a good doping range. So, it has a wide range of Plasmon Tuning from near IR to mid IR [86].

Indium Tin Oxide (ITO) is used as a good plasmonic material. The altering of oxygen content and metal atoms can control the plasmonic behavior [16].

4.5 Dielectric Materials

The PCF sensors use plasmonic materials on the outer surface for SPR phenomenon. The fiber is made of dielectric materials. The fiber has some holes in it in a specific pattern discussed earlier. In case of internal sensing they are filled with analytes where as in case of external sensing they are filled with air.

4.5.1 Silica

The most common dielectric used in PCF is Silica or Silicon Di Oxide. Many polymers are also used in PCF. But the Silica has a real value of RI which makes it desirable to use in PCF [87]. The undoped Silica is used for many reasons like-

- High optical nonlinearity
- Chemical Stability making the PCF reusable
- Stability in high temperature
- Excellent Mechanical Strength
- Higher damage threshold

- Large numerical Aperture upto 1, that allows more light to propagate through fiber in wide wavelength range

The RI of Silica can be found from the Sellmeir equation given below

$$n_{silica}(\lambda)=\sqrt{1+\frac{B_1\lambda^2}{\lambda^2-C_1}+\frac{B_2\lambda^2}{\lambda^2-C_2}+\frac{B_3\lambda^2}{\lambda^2-C_3}} \quad (4)$$

Where n_{silica} depends on wavelengths of light and temperature. This equation is valid for 0.22 μm to 3.71μm. The values of the Sellmeir constants are [63] -

Table 4.5.1 *Values of Sellmeir constants*

Constant	Value
B_1	0.69616300
B_2	0.407942600
B_3	0.897479400
C_1	0.00467914826 μm^2
C_2	0.0135120631 μm^2
C_3	97.9340025 μm^2

4.5.2 Air

The holes in the PCF are created to make the propagation and coupling of the light more efficiently. They are filled with Air. Air has a Refractive Index of 1 and the RI varies with the light wavelength in a very small scale close to 1. Sometimes the air holes are different in size and radius. The gap from one airhole center to another air hole center is called the pitch.

4.6 Multianalyte Sensor

There has been proposition of multianalyte sensors too. Until now we discussed about sensors that can detect single analytes. In June 2020, Firoz Haider proposed a design that can detect multianalytes. It is a grapefruit PCF based sensor that has three channels of analytes. There are 6 grapefruit sized holes in the center in a circular manner. In this sensor, internal sensing has been introduced. The holes are filled with three fluids. For increasing the Coupling between the SPP and core mode, Gold is used as plasmonic material. It has been introduced with mode multiplex phenomenon and due to this the sensor had polarization dependency.

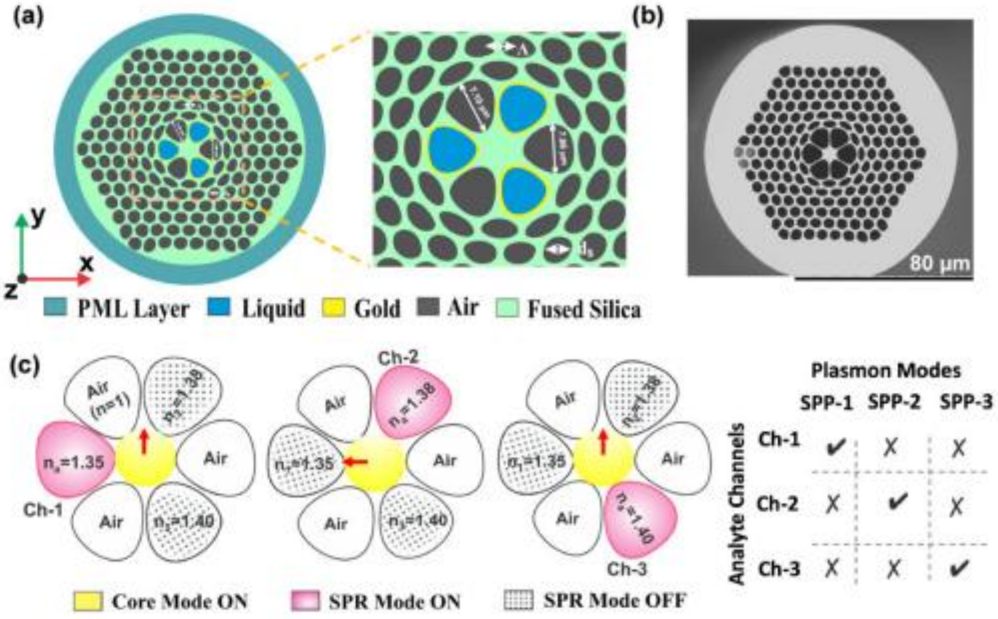

fig. 4.6 *(a) Schematic of grapefruit PCF sensor (b) SEM of the grapefruit PCF (c) Working mechanism of multiplex multi analyte PCF through core and spp mode*

The sensitivities of the three channels were observed 2000, 3000 and 18000 nm/RIU in 1.34,1.36 and 1.41 respectively which is good. The ability to simultaneously detect multi analytes in this PCF, contributed in many bio-recognition field [88].

4.7 Analyte Classification

In PCF sensor, for detecting a target molecule in the analyte there is a specific recognition layer on the surface of metal. The target molecule only works for that biorecognition molecule. When the resonance occurs the RI near the surface reduces and the target molecules are stuck in the sensor surface. The recognition molecules can be Proteins, Enzymes, Nucleic acid, DNA etc. Many target molecules like dissolved gases, nucleic acid, microorganisms, biomarkers, hormones, nucleoprotein etc can be detected. Medical diagnosis, disease detection and virus detection in blood sample etc are some of the applications of target molecule detection. Also, various target molecules have various RI. So, each PCF sensor can detect various target molecules according to its sensing range [11], [89].

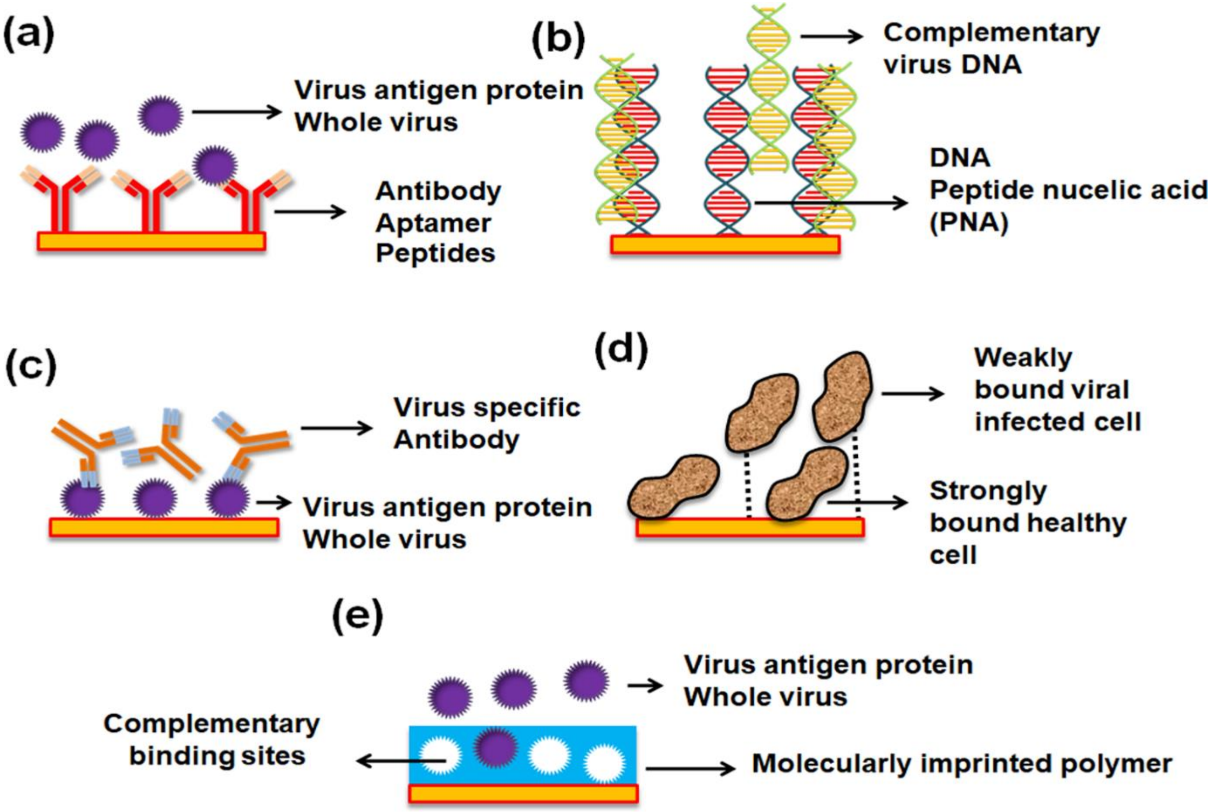

fig. 4.7 *Different target molecules detection using various bio-recognition molecules*

Chapter 5

Proposed Design: Ultra-Sensitive SPR sensor for multipurpose sensing

5.1 Introduction

This chapter has discussed on our proposed design on an ultra-sensitive Surface Plasmon Resonance-based Photonic Crystal Fiber (SPR-PCF) sensor that can be employed for multipurpose sensing of analyte, temperature, and magnetic field. Inside the fiber, our prototype contains a trigonal cluster-based strategic arrangement of circular air holes that can be easily fabricated using the traditional Stack-and-Draw process. Thin layers of gold (Au) and titanium dioxide (TiO_2) are used as the plasmonic materials surrounding the PCF. The sensor characteristics are estimated using the commercial program COMSOL Multiphysics 5.3a's Finite Element Method (FEM). We achieved a maximum Amplitude Sensitivity (AS) of 7223.62 RIU^{-1}, a maximum wavelength sensitivity (WS) of 28,500 nm/ RIU, and a leading figure of merit (FOM) of 914 RIU^{-1} after optimizing various parameters. With sensor resolutions of 1.38×10^{-6} (amplitude) and 3.51×10^{-6} RIU (wavelength), our sensor can detect unknown analytes in the refractive index (RI) range of 1.33 to 1.42. It can also detect temperature and magnetic field fluctuations with sensitivity levels of 1.25 nm/°C (1250 pm/°C) and 0.16 nm/Oe (160 pm/Oe), respectively. For the ±10% fabrication tolerance analysis, an infinitesimal difference in sensor performance was detected. As a result of its superior detecting capabilities and diverse characteristics, it can be inferred that this sensor may make a substantial contribution to scientific, biomedical, and industrial domains.

5.2 Schematic Modeling

The Stack-and-Draw approach was used to develop our suggested sensor in such a way that it can be simply produced. The bulk material for the PCF core was chosen to be silica. A trigonal design of air hole clusters has been strategically put inside the PCF to increase its sensitivity during detection of unknown analytes. **fig. 5.1(a)** and **fig. 5.1(b)** show the 2D cross section and 3D schematic diagram of the proposed design, respectively. To create each trigonal-shaped cluster, two types of airholes with dimensions of d_1 = 0.85 m and d_2 = 0.80 m were employed. Six clusters are symmetrically positioned at 60 degrees with each other inside the fiber, as shown in **fig. 5.1.(a).** These clusters are important in keeping the EM wave contained in the core. EM waves leak from the center and travel towards the metal through the channels between the clusters. The distance between two adjacent air holes' centers is known as pitch (*p*), which has a numerical value of 0.95 μm. Because of its better stability and huge RW shifts, gold was chosen as the plasmonic material in our concept [90]. The gold coating width, represented by tg, was optimised to a value of 20 nm. When a very thin coating of Au is put, however, there is a substantial risk that it will flake off the glass layer. [63]. An extra layer of TiO_2 was put between the silica and gold coating to solve the adhesion problem. This thin TiO_2 coating also aids in the development of a robust coupling between the guided core and surface plasmonic mode. The TiO_2 thickness (t_t) was tuned to be 15 nm. A 1.20 μm thick channel was built outside the Au layer through which the unknown analytes to be diagnosed were passed. The thickness of the analyte layer has a negligible effect on the sensor's sensitivity [91]. To confine the computational domain, we developed a Perfectly Matched Layer (PML) at the outermost surface. The PML that surrounds the fiber offers anti-reflectivity and guarantees that scattered evanescent fields are absorbed rather than reflected into the limited area [91], [92]. The PML layer is absent in a practical sensor as it is employed only for better simulation purposes [91] . In our design, we chose the thickness of the PML layer to be t_{PML} = 1.40 μm.

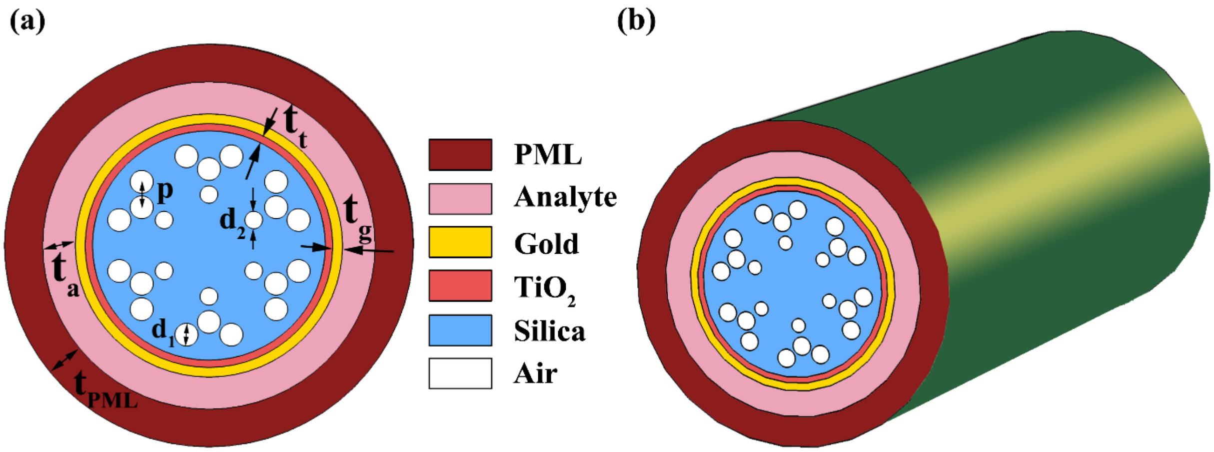

fig. 5.1 *(a) 2D Schematic cross section, (b) 3D Fiber tube.*

5.3 Fundamental mode field profile

When light is transmitted through the PCF's center, an amplified evanescent field is formed in the core, which is known as the core mode. The airholes seek to restrict the core's evanescent field. However, through the channels between the air hole clusters, a component of this evanescent field seeps from the core. The surface plasmon polariton (SPP) mode is formed when the leaking field interacts significantly with the metal. The core and SPP modes for x and y polarized incident photons are shown in **fig. 5.2**.

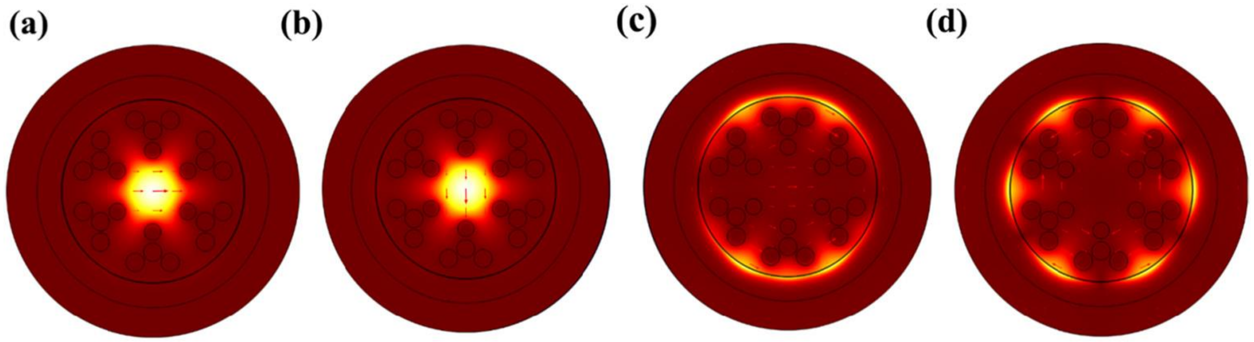

fig. ***5.2*** *Fundamental mode field profile of core mode for (a) x-pol, (b) y-pol; and SPP mode for (c) x-pol, (d) y-pol.*

5.4 Dispersion and stacked preform

As seen in **fig. 5.3(a),** the highest loss occurred at the wavelength 0.625 m, when both the core and SPP modes had the same effective RI values. Both x-pol and y-pol showed nearly identical confinement loss. As a result, we choose to optimize the sensor parameters for x-pol only. The stacked preform construction of our proposed sensor is shown in **fig. 5.3(b).** The hexagonal lattice of the PCF may be formed by stacking different types of capillary rods (solid, thin wall, and thick wall rods).

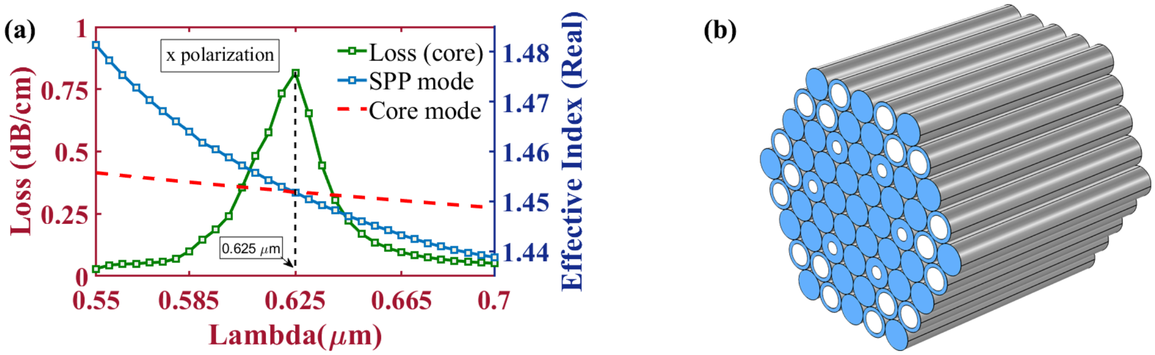

fig. ***5.3*** *(a) Phase matching of x-polarization (b) Stacked preform structure*

.

5.5 Gold (Au) and TiO_2 film thickness optimization

The gold layer thickness t_g is used to start the parameter optimization process, followed by TiO2 thickness t_t. Because the gold layer generates surface plasmon waves (SPW), it has a significant influence on the sensor's output. Because of its high RI, the TiO_2 layer acts as a transition metal, drawing the evanescent field from the center [93]. By forcing electrons to propagate at the surface, the TiO_2 layer increases sensor performance [91]. As a result, a strong coupling between the core guided and surface plasmonic modes is formed. Initially, we considered t_a = 1.20 µm, t_{PML} = 1.40 µm, t_t = 10 nm, d_1 = 0.9 µm and d_2 = 0.8 µm. While altering the gold film thickness, we maintained these parameters constant. We changed the wavelength of t_g to 15 nm, 20 nm, and 25 nm. The CL and AS characteristics are shown in Figs. 6.1 (a) and 4 (b). CL is roughly comparable for 20 nm and 25 nm, as can be shown. However, because t_g = 20 nm had the greatest AS (727.16 RIU^{-1}), we decided that 20 nm was the best gold coating thickness. The thickness of TiO_2 was changed to 10 nm, 15 nm, and 20 nm in the next stage, while the gold coating thickness was fixed to 20 nm. The CL and AS curves are shown in **fig. 5.5 (c)** and **5.5(d).** A thicker TiO_2 layer, naturally, leads in a higher CL. A thick layer, on the other hand, prevents the analyte from interacting with the evanescent field, lowering sensitivity. So, we choose 15 nm as our optimized value of TiO_2 film thickness and got corresponding AS of 728.63 RIU^{-1} which is the maximum.

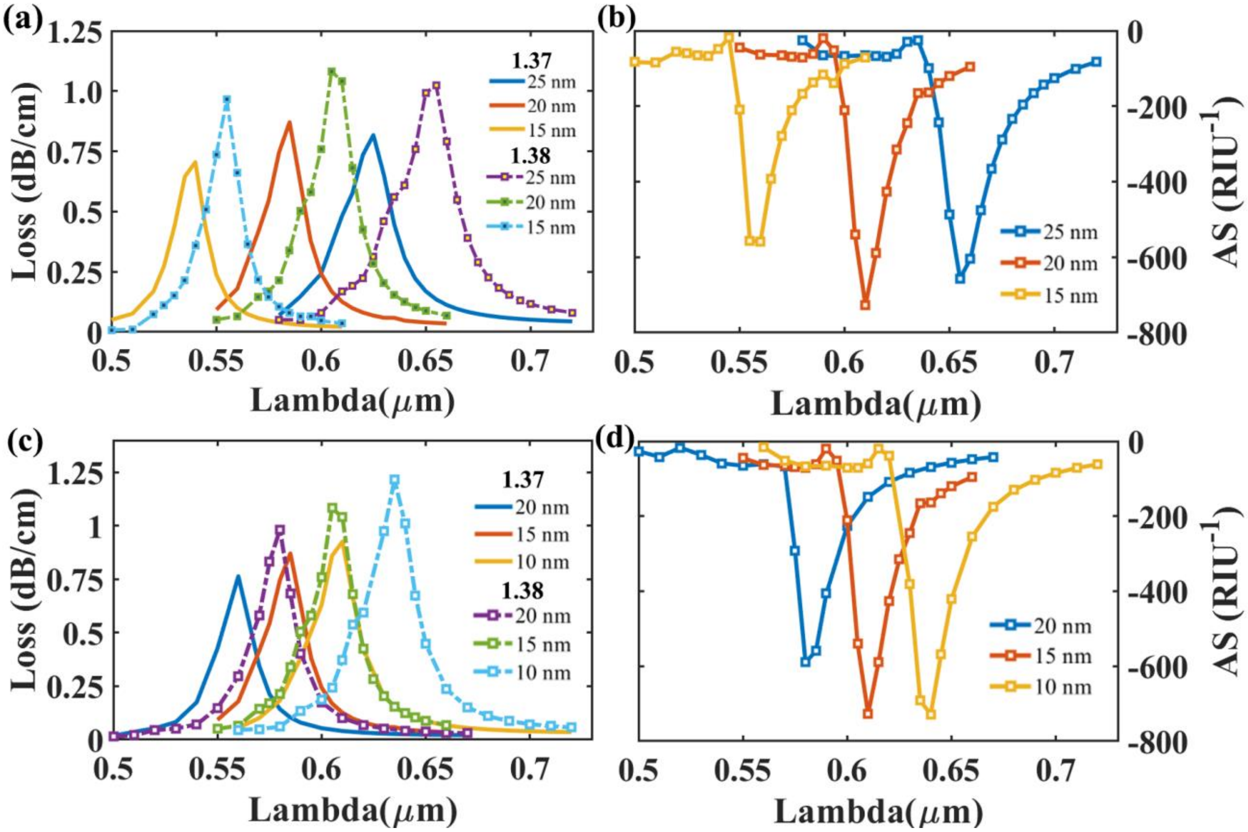

fig. 5.5 *(a) CL curves for environment RI of 1.37 and 1.38 at* t_g *= 15 nm, 20 nm, 25 nm (b) AS curves at* t_g *= 15 nm, 20 nm, 25 nm (c) CL curves for environment RI of 1.37 and 1.38 at* t_t *= 10 nm, 15 nm, 20 nm (d) AS curves at* t_t *= 10 nm, 15 nm, 20 nm.*

5.6 Pitch (*p*) and air hole diameters (d_1 & d_2) optimization

The pitch is the distance between the centers of two adjacent air holes. Pitch influences a variety of parameters, hence it has a significant impact on sensor efficiency. The initial pitch value in our concept was 1.00 μm. This value was changed to 1.05μ m and 0.95 μm. 762.572 RIU^{-1}, 728.63 RIU^{-1}, and 735.116 RIU^{-1} are the AS for pitch values of 0.95 m, 1.00 m, and 1.05 m, respectively. The CL is lowered at lower pitch values because the clusters are closer together at lower pitch values. This enables improved EM wave containment, leading in a superior AS [63]. So, we took 0.95 μm as our optimized pitch value. The consequences of changing pitch are demonstrated in **fig. 5.6 (a)** and **5.6 (b).** The effect of changing air hole diameter d_1 is displayed in **fig. 5.6 (c)** and **5.6 (d).** Because light confinement declines with smaller air holes, the CL is higher for smaller diameters. When d_1 is dropped to 0.85 m, however, the AS rises from 762.572 RIU^{-1} (for 0.90 μm) to 775.981 RIU^{-1}. For 0.80 μm, we saw a decrease in AS. As a result, 0.85 μm was chosen as the optimal d_1. In the instance of d_2, we started with 0.8 μm because it produced the greatest results. As a result, d2 optimization is not necessary.

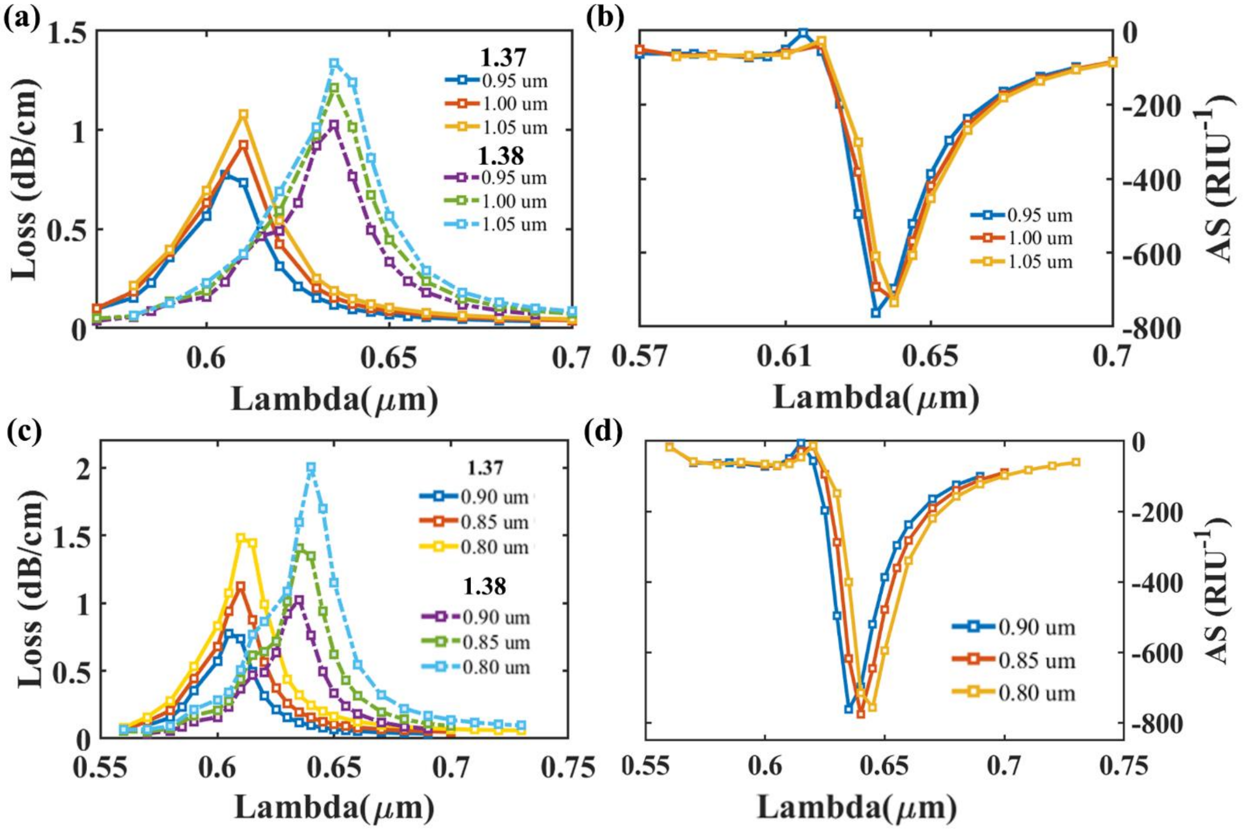

fig. 5.6 *(a) CL curves for environment RI of 1.37 and 1.38 at p = 0.95 μm, 1.00 μm and 1.05 μm (b) AS curves at p = 0.95 μm, 1.00 μm and 1.05 μm (c) CL curves for environment RI of 1.37 and 1.38 at d_1 = 0.90 μm, 0.85 μm and 0.80 μm (d) AS curves at d_1 = 0.90 μm,*

5.7 Analyte sensing of our proposed design

The CL and AS behaviors with the variation in analyte RI are shown in **fig. 5.7 (a)** and **5.7 (b)**, respectively. The suggested sensor has a high sensitivity while maintaining a low CL, as can be shown. 545 nm, 555 nm, 570 nm, 590 nm, 610 nm, 635 nm, 675 nm, 725 nm, 805 nm, 960 nm, and 1245 nm are the resonance wavelengths for analyte RI 1.33 to 1.43, respectively. As EM field penetration towards the core diminishes and penetration towards the SPP mode grows, the CL increases with RI [94]. At analyte RI 1.41, a maximum AS of 7223.6258 RIU^{-1} was attained, whereas at analyte RI 1.42, a maximum WS of 28,500 nm/ RIU was observed coupled with a sharp resonance peak. As can be observed in Fig. 7 (a), the CL peak increased significantly for analyte RI values greater than 1.42, resulting in a reduced AS of roughly 4366 RIU^{-1} as shown in fig. 7(b). As a result, in the case of higher RI values, there is a risk of erroneous detection. As a result, we specified a RI range of 1.33 to 1.42 for our sensor. For the RI range of 1.33 to 1.42, our sensor had FWHM values of 20.9, 21.98, 22.8, 24.9, 25.8, 24.1, 23.5, 24.9, 28.8, and 31.2. We found a maximum sensor resolution of 3.51×10^{-6} for wavelength and 1.38×10^{-6} for amplitude using $\partial\lambda_{min}$ = 0.1 nm. As a result, it can be assumed that the suggested sensor can detect RI variations in the order of 10^{-6}. Using numeric analysis, we obtained a maximum FOM of 914 for both polarizations. The FOM gives an understanding of a sensor's overall performance, and a larger FOM suggests a higher detection threshold [95]. Our suggested sensor has a very high FOM, which makes it more appealing. **Table 5.7.1** shows the performance evaluation findings based on the aforementioned factors. **Table 5.7.2**, on the other hand, compares our sensor to other sensors that have been described thus far.

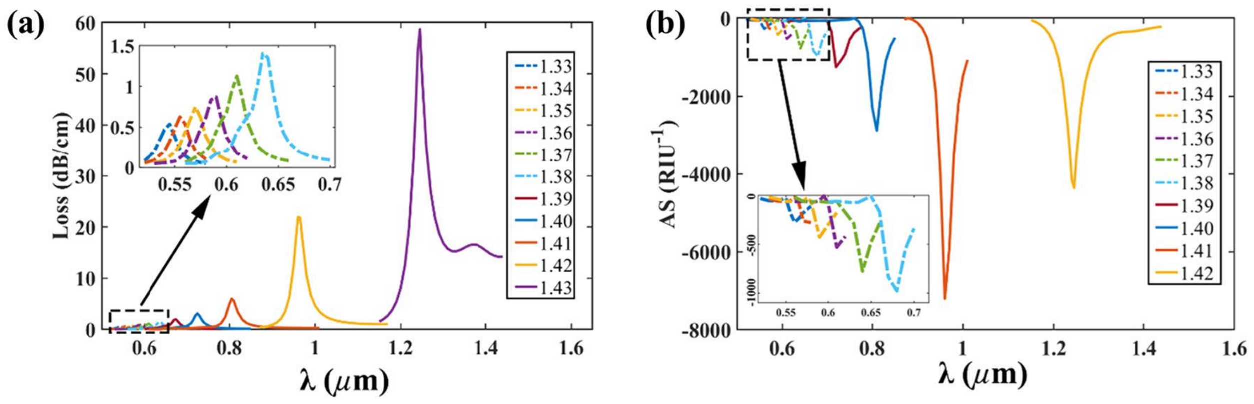

fig. 5.7 *(a) CL curves for x-pol at analyte RI of 1.33 to 1.43 and (b) AS curves for x-pol at analyte RI of 1.33 to 1.42 at optimized parameters.*

Table 5.7.1 *Performance analysis of the proposed sensor with varying dielectric RI*

RI	RW (nm)	AS(RIU^{-1})		Amplitude resolution (RIU) (×10^{-6})		WS (nm/RIU)	Wav. Res (RIU)(×10^{-6})	FWHM		FOM	
	x & y pol	x pol	y pol	x pol	y pol	x & y pol	x & y pol	x pol	y pol	x pol	y pol
1.33	545	274.8	274.7	36.4	36.4	1000	100	20.94	20.95	47.8	47.7
1.34	555	341.3	341.2	29.3	29.3	1500	66.7	21.97	21.98	68.3	68.3
1.35	570	426.9	426.7	23.4	23.4	2000	50.0	22.83	22.85	87.6	87.5
1.36	590	545.3	544.9	18.3	18.3	2000	50.0	24.85	24.87	80.5	80.4
1.37	610	776	775.5	12.8	12.8	2500	40.0	25.79	25.85	97	96.7
1.38	635	1105.5	1104.9	9.04	9.05	4000	25.0	24.05	24.06	166.3	166.3
1.39	675	1678.3	1677.6	5.96	5.96	5000	20.0	23.51	23.52	212.7	212.6
1.40	725	2933.8	2933	3.40	3.40	8000	12.5	24.92	24.92	321	321
1.41	805	7223.6	7218	1.38	1.38	15,500	6.45	28.83	28.83	537.6	537.7
1.42	960	4366.1	4365.5	2.29	2.29	28,500	3.51	31.16	31.16	914.6	914.7
1.43	1245	-	-	-	-	-	-	-	-	-	-

Table 5.7.2 *Comparison of different parameters between the proposed and other reported sensors*

Reference	AS(RIU^{-1})	Amplitude resolution (RIU)	WS (nm/RIU)	Wav. Res (RIU)	FOM
[96]	6829	5×10^{-6}	28,000	3.57×10^{-6}	2800
[90]	4358.09	2.29×10^{-6}	21,000	4.76×10^{-6}	729
[97]	1757.3	-	32,000	1.428×10^{-6}	587.2
[63]	1411	-	25,000	4×10^{-6}	502
[67]	1680	-	216,000	4.63×10^{-6}	1200
[98]	1872	9.09×10^{-6}	51,000	1.96×10^{-6}	566
[99]	2050	-	111,000	9×10^{-6}	-
[100]	4738.9	2.11×10^{-6}	14,500	6.9×10^{-6}	387
[93]	4596	2.18×10^{-6}	17,000	5.88×10^{-6}	-
[91]	5060	1.98×10^{-6}	41,500	2.41×10^{-6}	1068.7
This paper X pol	7223.62	1.38×10^{-6}	28,500	3.50×10^{-6}	914.58
Y pol	7218.00	1.38×10^{-6}	28,500	3.50×10^{-6}	914.70

5.8 Temperature sensing of our proposed design

Due to the extremely temperature-dependent propagation modes of PCF, several PCF-based SPR sensors have been applied in the field of temperature sensing. [101]. Our suggested sensor may also be employed as a temperature sensor when the analyte is ethanol, a temperature-sensitive substance. The RI of ethanol changes as a result of temperature change, causing a considerable shift in the RW. The equation of ethanol's RI with temperature variation is [91]:

$$n_1 = n_0 + \frac{dn}{dT}(T_1 - T_0) \tag{5}$$

The RI at temperatures T_0 and T_1 are denoted by n0 and n1, respectively, and the thermo-optical coefficient of ethanol is denoted by $dn/dT = -3.117\times10^{-4}\,^{\circ}\mathrm{C}^{-1}$. The RI of ethanol is $n_0 = 1.361$ at $T_0 = 20\,^{\circ}\mathrm{C}$. Ethanol has a melting point of -114.1 °C and a boiling point of 78.37 °C. The RI of ethanol in the liquid form ranges from 1.343 to 1.403 depending on temperature. As a result, the RI of liquid ethanol remains within the detection range of our sensor at any temperature. As a result, our sensor can detect minor external temperature differences utilizing ethanol. The confinement loss vs. wavelength curves at various temperatures are shown in **fig. 5.8 (a)**. It is obvious that when the temperature rises, the resonant wavelength shifts to the left. A third-order fitting (R2 = 0.99997) relationship between a collection of temperatures and their associated resonant wavelengths is depicted in **fig. 5.8 (b).** The fitting curve can be mathematically expressed using the following equation:

$$y = 603.1875 - 0.71999x + 0.003006x^2 - 1.3258\times10^{-0.5}x^3 \tag{6}$$

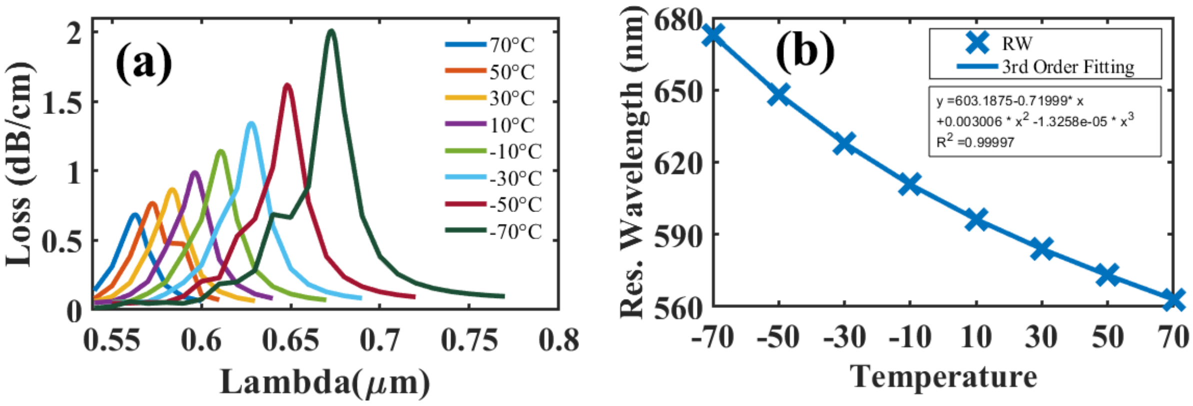

fig. 5.8 *(a) CL curves for different temperatures; (b) Resonant Wavelength vs. Temperature curve for a range of -70 ◦C to 70 ◦C.*

Here, y stands for the RW in nm, and x identifies the temperature. The resonance wavelength may be retrieved from the spectrum analyzer at any unknown temperature, and the temperature can then be estimated using suitable equation. **Table 5.8.3** shows the measured temperature sensing parameters of our proposed sensor. It demonstrates a maximum sensitivity of 1.25 nm/˚C (1250 pm/˚C). The average sensitivity is calculated to be 0.7857 nm/˚C (785.7 pm/˚C). The maximum resolution is 0.08 ˚C. These values indicate an outstanding temperature sensor capability across a wide temperature range. The performance of the suggested temperature sensor is compared to that of previously reported sensors in **Table 5.8.4**. Along with analyte detection, this sensor offers outstanding temperature detection capabilities, opening up new possibilities in the field of temperature sensing.

Table 5.8.3 *Performance analysis of the proposed sensor with varying temperature.*

Temperature (ºC)	Resonant wavelength (µm)	Sensitivity (nm/ ºC)	Resolution	Average sensitivity
-70	0.673	1.25	0.08	0.7857
-50	0.648	1	0.1	
-30	0.628	0.85	0.117647059	
-10	0.611	0.75	0.133333333	
10	0.596	0.6	0.166666667	
30	0.584	0.55	0.181818182	
50	0.573	0.5	0.2	
70	0.563	-	-	

Table 5.8.4 *Comparison between the proposed temperature sensor and other reported sensors.*

Reference	Sensitivity (nm/ ºC)	Resolution (ºC)	Sensing range
[91]	0.229	0.437	25 ºC to 55 ºC
[91]	0.75	0.133	-70 ºC to 70 ºC
[102]	0.978	0.102	25 ºC to 100 ºC
[103]	1.00	0.1	-70 ºC to 70 ºC
[104]	1.16	0.86	35.5 ºC to 70.1 ºC
[105]	1.551	0.064	35 ºC to 100 ºC
[106]	110	0.00091	10 ºC to 70 ºC
This paper	1.250	0.08	-70 ºC to 70 ºC

5.9 Magnetic field sensing of our proposed design

As previously prescribed, when the Magnetic Fluid (MF) is utilized as the analyte, our sensor may also be used for magnetic field detection. Langevin function describes the relationship between the MF RI and the applied magnetic field, and it can be expressed as [107]:

$$n = [n_s - n_l][\coth(\alpha \frac{H - H_{c,n}}{T}) - (\frac{T}{\alpha(H - H_{c,n})})] + n_l \tag{7}$$

Here, H denotes magnetic field strength (Oe), T denotes temperature (Kelvin), and denotes the fitting parameter. The critical field's strength, RI for fields less than $H_{c,n}$, and saturated RI value are denoted by $H_{c,n}$, n_l, and n_s, respectively.. For our analysis, the corresponding values of n_s = 1.3901, T = 20 ºC, α = 0.143, and n_l = 1.3411 [107]. To measure the sensor's magnetic field sensing performance, an external magnetic field must be applied and calibrated properly. For this, a magnetic coil and a gauss-meter can be used [108]. Because the surrounding temperature may change during sensing, the temperature-dependent RI of MF complicates precise detecting the magnetic field. To accurately measure the magnetic field, an appropriate temperature adjustment method is required. This problem may be solved by considering the temperature dependency of MF RI. For a zero magnetic field, the temperature dependency may be discovered by watching the RW change caused by any change in ambient temperature. Any anomalous change in RW during magnetic field measurements suggests a temperature influence, which may be studied and adjusted using temperature dependency information. Attaching a fiber-Bragg-grating (FBG) based grating component to the magnetic field probe is another technique of compensating [107]. If $\Delta\lambda_{peak}$ denotes the loss peak drift distance and ΔH denotes the magnetic field change, the magnetic field sensitivity of the sensor can be quantified as [109]:

$$S_H = \frac{\Delta\lambda_{peak}}{\Delta H}(nm / Oe) \tag{8}$$

Magnetic field strengths of 0, 125, 250, 375, 500, 625, 750, 875, and 1000 Oe were used to analyze the magnetic field sensor characteristic. As the field strength was raised, there was a red-shift in the RW. Within this field strength range, the RW moved from 545 nm to 645 nm, as seen in **fig.**

5.9. (a). A fourth-order fitting (R2 = 0.99821) connection between magnetic field strength and RW is shown in **fig. 5.9 (b).** When x signifies the magnetic field strength (Oe) and y specifies the resonance wavelength (nm), the fitting curve can be mathematically expressed using the following equation:

$$y = 545.2797 + 0.11678x + 0.00034126x^2 - 7.1608e^{-7}x^3 + 3.5804 \times 10^{-10}x^4 \quad (9)$$

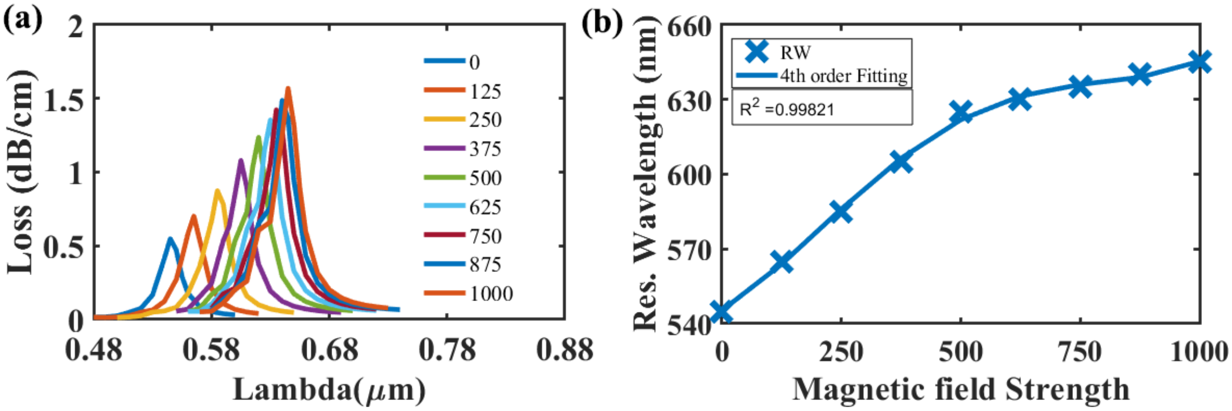

fig. 5.9 (a) CL curves for different applied magnetic field intensities (b) Resonant Wavelength vs. Magnetic field strength in a range of 0 to 1000 Oe.

Our sensor's magnetic field sensing parameters are presented in **Table 5.9.5**. The maximum magnetic field sensitivity of our sensor is 0.16 nm/Oe (160 pm/Oe), with an average sensitivity of 0.1 nm/Oe (100 pm/Oe). 0.625 Oe is predicted to be the maximum resolution. **Table 5.9.6** compares the performance of our sensor to that of other magnetic field sensors previously published. In comparison to the majority of current sensors, our sensor performs admirably, as shown in **Table 5.9.5** and **Table 5.9.6**.

Table 5.9.5 *Magnetic field sensing performance of the proposed sensor*

Magnetic Field strength (Oe)	**Resonance Wavelength(μm)**	**Sensitivity (nm/Oe)**	**Resolution (Oe)**	**Average Sensitivity (nm/Oe)**
0	0.545	0.16	0.625	0.10
125	0.565	0.16	0.625	
250	0.585	0.16	0.625	
375	0.605	0.12	0.833	
500	0.62	0.08	1.250	
625	0.63	0.04	2.500	
750	0.635	0.04	2.500	
875	0.64	0.04	2.500	
1000	0.645	-	-	

Table 5.9.6 *Comparison between the proposed magnetic field sensor and other reported sensors*

References	**Sensitivity (nm/Oe)**	**Resolution (Oe)**	**Sensing Range**
[110]	0.041	2.439	0 to 250
[109]	0.061	1.639	50 to 130
[111]	0.092	1.087	0 to 100
[112]	0.143	0.699	0 to 350
[113]	1.063	0.094	30 to 210.9
This paper	0.16	0.625	0 to 1000

5.10 Methods of fabrication

Because we used a simulation to evaluate our sensor's performance, we need to look into the possibility of constructing this structure. The outstanding results of this numerical analysis will be irrelevant if the sensor construction is not fabricable in reality. As a result, we provide approaches for developing our sensor. We must first create the PCF framework before laminating it with plasmonic materials. Our sensor has been designed such that the PCF may be simply produced utilizing the stack-and-draw approach. Capillaries are piled together to form a certain lattice structure, and then drawn using a drawing tower to construct the PCF in the stack-and-draw method [114]. Three types of capillary rods (solid, thick-wall, and thin-wall) can be used to build the hexagonal lattice stacked preform of our sensor PCF, shown in **fig. 5.3 (b).** During the preform stage, drill the rods using an ultrasonic mill to create the needed round air holes [15]. Wiederhecker et al. employed the stack-and-draw approach to make a PCF with air-hole diameter and pitch of 110 nm and 650 nm, respectively [115]. Our suggested PCF has larger air hole sizes (800 nm, 850 nm) and pitch (950 nm) than their PCF. As a result, there is no question that the Stack-and-Draw approach may be used to easily build the PCF for our sensor. The PCF structure must then be laminated with the required plasmonic materials once it has been formed (gold and TiO2). The thin laminations surrounding the PCF can be applied using a variety of ways. Electron beam evaporation, chemical vapor deposition (CVD), wheel polishing, atomic layer deposition (ALD), and high-pressure microfluidic chemical deposition are some of the most dependable processes [34,39]. Since Li et al. constructed an SPR sensor with a 35 nm thick gold layer formed by electron beam evaporation, the thin plasmonic films of our sensor are practically possible with the use of existing deposition technologies [116]. As a result, we may infer that all of the current manufacturing methods are capable of fabricating our sensor.

5.11 Fabrication tolerance investigation

Although existing approaches can build our sensor, it is unclear if the PCF dimensions can be maintained exactly. In a real scenario, we generally face ±1–2% deviations from the desired parameters while fabricating the sensor [96]. As a result, if the intended PCF dimensions are not reached, sensor performance, which is a function of geometrical factors, is most likely to be altered. As a result, a fabrication tolerance analysis is required to forecast sensor performance deterioration due to incorrect fabrication. We investigated how sensor performance changed when d_1 and d_2 were ±5% and ±10% from their optimal values, respectively. **fig. 5.(a)** depicts the effect of d1 variation on the CL, whereas **fig. 5.(b)** depicts the influence of d_2 variation on the CL. We can observe that the RW stays the same for a -5% change in d_1 and deviates somewhat by 5 nm for +5 percent and ±10% changes. For a -10% divergence in d_2, however, the RW only perceives a 5 nm shift. The sensor's performance will not be affected by these little fluctuations in RW. As a result, we can definitely state that our design can withstand manufacturing mistakes of up to ±10% without adversely affecting sensor performance.

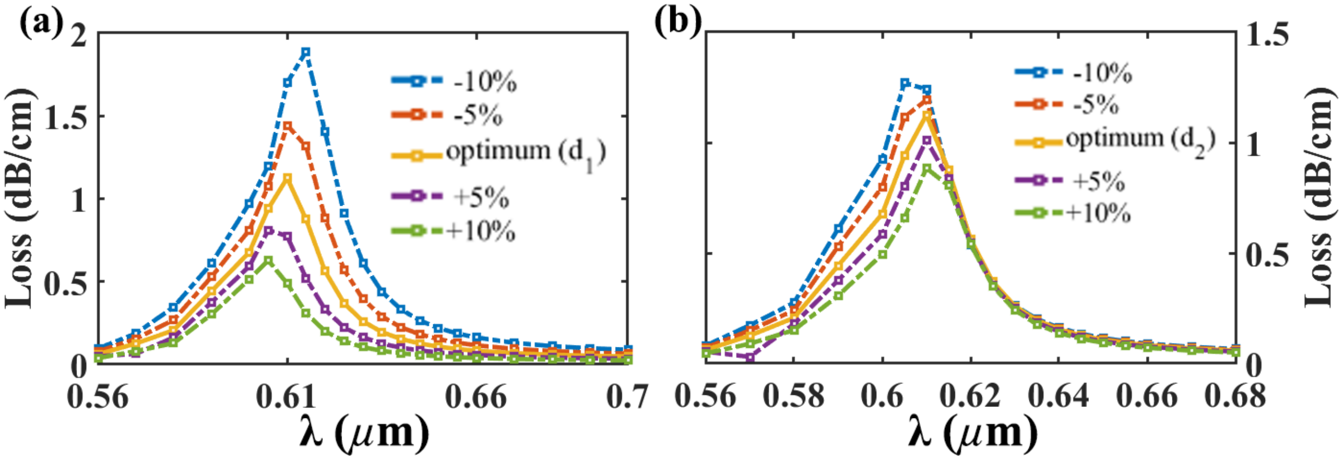

***fig. 5.11** CL curves at analyte RI 1.37 with ±5% and ± 10% variation in (a) parameter d_1, and (b) parameter d_2.*

5.12 Explanation of improved performamce

The mutual interaction between the evanescent field and the plasmonic metal influences the sensor performance. The pathways via which light escapes from the core and propagates towards the plasmonic layer play a significant role in this mutual interaction. As a result, a broader channel is expected to allow for greater interaction between the plasmonic layers and the analyte, resulting in increased sensitivity. The overall angle they produce at the center of the PCF can be used to describe channel width. We developed a relationship between the AS and the total channel angle for numerous sensors based on careful observation. **fig. 5.12** depicts those sensor structures, where the channels are outlined by arrows from the center of the sensor. **fig. 5.12** illustrates the relationship between the AS and the total channel angle and clearly indicates that the AS improves with the increase in total channel angle. Light may easily flow towards the cladding and interact with the plasmonic metal due to the broad channel angle. Sensors with broad channel angles are intended to have great sensitivity. As a result, we were inspired to build our sensor with a larger channel angle while still adhering to the stack-and-draw manufacturing method. For the PCF, we picked a hexagonal lattice structure and then strategically inserted air holes in it to produce the six channels. We discovered that utilizing trigonal clusters of air holes improves the channel angle (102 degrees) while maintaining sufficient light confinement at the core. Our sensor's unique trigonal cluster-based layout, increased channel angle, manufacturing practicality, improved performance, and multipurpose application potential make it distinctive. Although our data indicate that a broader channel is linked to a higher AS, this is not always the case. On the other

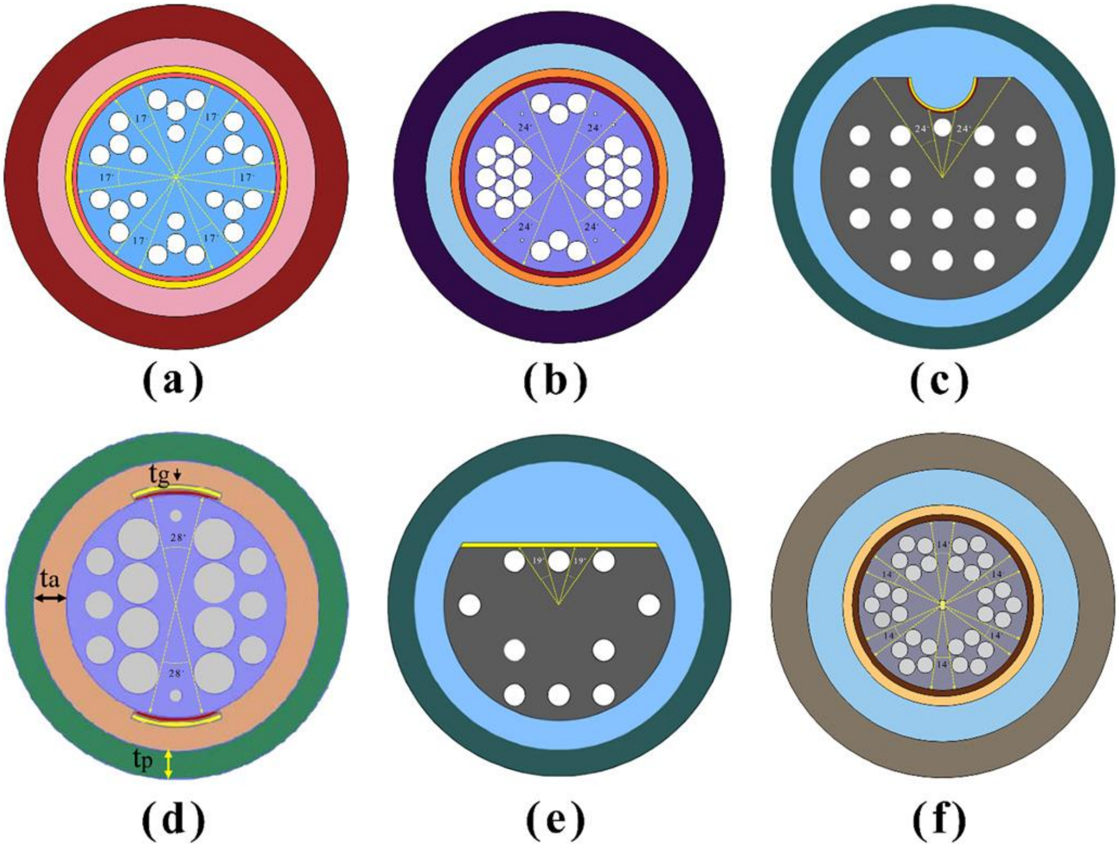

fig. 5.12 *Channel highlighted sensor structures of (a) this work, (b) ref.[91], (c) ref. [98], (d) ref.[99], (e) ref.[117], (f) ref.[93].*

hand, a large channel may compromise light confinement in the core. As a result of the increased signal loss, sensor efficiency may suffer.

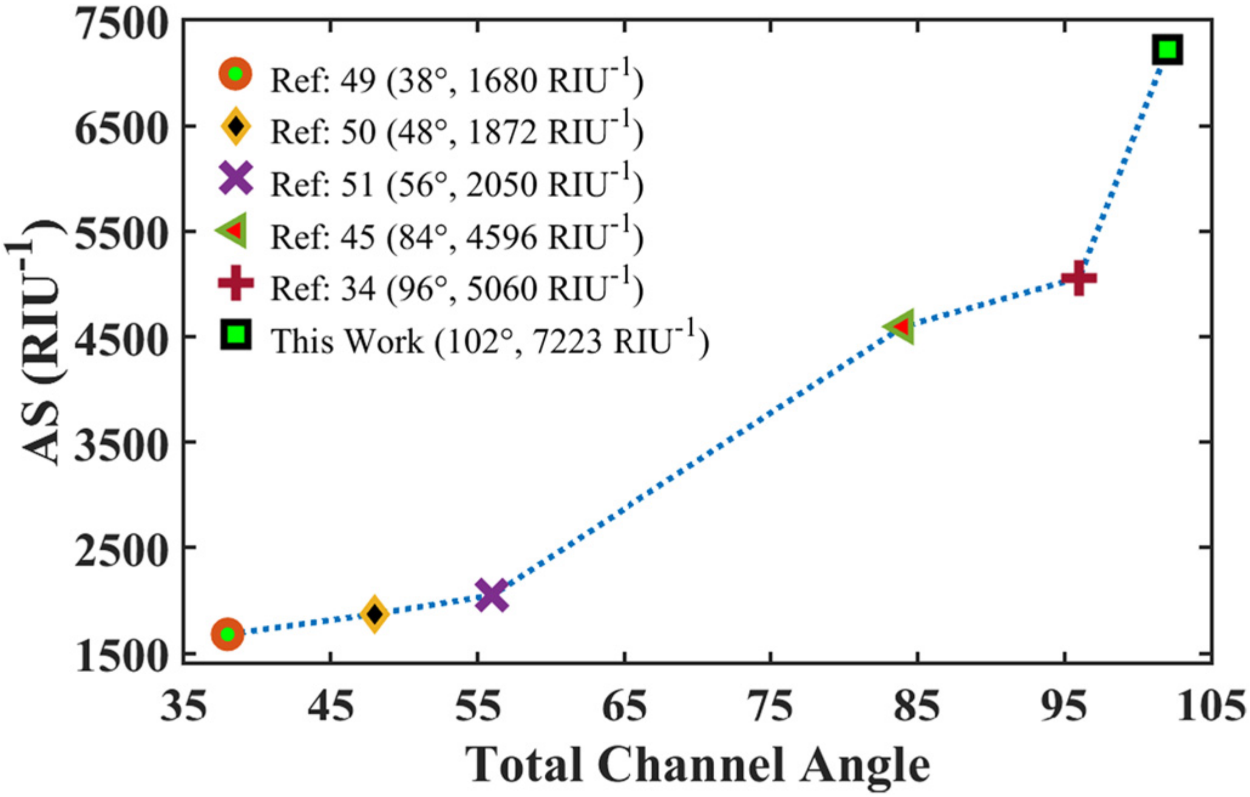

fig. 5.13 *Amplitude Sensitivity of different sensors vs. total channel angle.*

5.13 Suitable analysis for sensing

The ability to use SPR sensors for a multitude of applications is the fundamental reason for their appeal among scientists. When temperature-sensitive ethanol or magnetic field-sensitive fluid is employed as the analyte, our suggested sensor may be used as a temperature or magnetic field sensor, as mentioned in the previous sections. Furthermore, following suitable surface functionalization, this sensor may detect any target molecule [118]. To detect a specific target molecule, a biorecognition molecule specific to that molecule can be placed on the sensor surface, allowing only that molecule to access the sensor surface. Antibodies, nucleic acids, peptides, enzymes, DNA, and lectins are examples of biorecognition molecules [118], [119]. After proper surface functionalization, our sensor will be able to detect a plethora of target molecules such as dissolved gases (methane, carbon dioxide), pollutants, trace metal ions (Cd, Zn, Ni, Cu2+), biomarkers, hormones, polycyclic aromatic hydrocarbons (benzo-[A]-pyrene), pesticides (simazine, atrazine), phenolic compounds (bisphenol A), pathogens, toxins (okadaic acid, domoic acid, staphylococcal enterotoxin B, saxitoxin family), nucleic acid, microorganisms (*Escherichia coli*, *Alexandrium minutum*, *Salmonella typhimurium*), nucleoprotein (NP) of H1N1 influenza virus solution and so on [118]–[121]. Furthermore, our sensor has been described to work in the RI range of 1.33–1.42. Apart from the aforementioned target molecules, our sensor can detect a wide range of critical biological agents and biochemical solutions with RIs in this range. Some of those prominent analytes are human intestinal mucosa (1.329–1.338), human urine concentration (1.3415–1.3464), 10% glucose solution (1.3477), blood plasma (1.35), White Blood Cell (1.36), ethanol (1.361), 20% glucose solution (1.3635), breast cancer cells (MDA-MB-231 and MCF-7) human liver (1.369), hemoglobin (1.38), adrenal gland cancer cell (PC12), cervical cancer cell (HeLa), blood cancer cell (Jurkat), skin cancer cell (Basal) (1.36–1.40), Red Blood Cell (1.40), ethylene tetrafluoroethylene (1.403), 50% sugar solution (1.42), and many more [91]. As a result, our sensor can work with a wide variety of chemical and biological analytes in both liquid and gaseous forms.

5.14 Maintaining excellent performance

Although our sensor performs admirably in numerical tests, things may differ in real-world situations, and we may not achieve the intended results. Sensor performance may be harmed as a result of any complexity or inaccuracy in sensor construction. However, in Section 5.10, we have discussed the fabrication feasibility of our sensor with the help of existing techniques. We have also shown in Section 5.11 that the effect of fabrication error on the sensor performance is negligible. Moreover, Wang et al. fabricated an SPR-based PCF sensor with a more complex structure than our sensor [105]. In comparison to our sensor (24), their PCF contains a lot of air holes (90). Despite the fact that their sensor has a temperature sensitivity equivalent to ours, their WS is inferior to ours. So, because our sensor has a lot simpler structure, we may anticipate it to work as planned because the production of this sensor will be straightforward. However, we recommend a few procedures in this section to guarantee that our sensor performs well in real-world applications. As mentioned in Section 5.13, our sensor can deal with a plethora of target molecules based on the type of surface functionalization used. The analyte-plasmonic metal interaction is another important aspect that determines sensor performance. As a result, we must maintain optimal surface functionalization and analyte flow to enable precise detection of target molecules in real-world applications. A programmable micro injection pumper (LSP01-1A, LongerPump^{TM}) may be used to inject sample solutions into the analyte channel [91]. We can control the flow rate of the analyte by using a pumper. For improved results, solutions might be routed through a mesh filter before being inserted into the sensing channel [118]. The flow channel should be washed with a buffer solution after each use to eliminate any remaining target molecules from the previous use. The biorecognition layer may erode or wear away over time, resulting in decreased sensing efficacy. As a result, the layer must be refreshed on a regular basis. By infusing a regeneration solution into the analyte channel, this regeneration is easily performed. These steps will enable optimal sample solution flow, improved contact with the sensing layer, and improved sensing performance.

5.15 Recommendations for future research and improvement

We propose a multifunctional sensor that can detect analytes, temperature, and magnetic field in this paper. When the sensor is used for one of the three functions, however, it cannot be used for the other two. Future studies might look into how to identify all three characteristics at the same time. Furthermore, future study might focus on using the sensor to detect additional characteristics. Due to the significant CL observed at higher wavelengths, our sensor's analyte detection range is restricted to RI of 1.42. The exorbitant losses at higher wavelengths result from Silica's optical transmission profile, which is confined up to a wavelength of 2.4 μm [122]. As a result, analytes with RI greater than 1.42 are undetectable by our sensor. Furthermore, this RI limit limits the temperature sensitivity of our sensor. We utilized ethanol as the analyte for temperature sensing since its temperature-dependent RI is within the RI range of our sensor. However, there are liquids with significantly greater thermo-optical coefficients (such as chloroform, toluene, and PDMS) that might have improved temperature sensitivity. However, we are unable to employ such liquids since their RI is beyond of our sensor's detection range. Replace the PCF material Silica with a material with a wide transparency window to fix these problems. Sapphire, fluoride glass, and chalcogenide glass (such as As_2Se_3) are some alternate materials with transparency windows of 6.0, 7.0, and 17.0 meters, respectively [122]. In the future, investigations can be done with these alternative materials to estimate the sensor performance for higher RIs.

5.16 Conclusion

This work was based on a circular gold coated SPR sensor. The main motivation was to design a sensor for multi-purpose sensing-unknown analyte, temperature and magentic field. The design was trigonal cluster SPR based PCF design. Gold and TiO_2 was used for their stable properties for unknown analyte sensing. For temperature sensing, Ethanol was used and magnetic sensing was done with Magnetic Fluid. For the high sensitivity and performance parameters, the structural parameters were optimized using COMSOL 5.3a with FEM method. After optimization the maximum AS was found 7223.62 RIU^{-1} and maximum WS was found 28500 $nmRIU^{-1}$ in the RI range 1.33 to 1.42. The sensor resolution was 1.38×10^{-6} for amplitude and 3.51×10^{-6} for wavelength. The maximum temperature and magnetic field sensitivities are 1.25 nm/°C & 0.16 nm/Oe respectively. The analysis for fabrication tolerance was done with ±10% deviation in all the structural parameters. This multi-purpose sensor with good results can help in many fields of SPR applications.

Chapter 6

Conclusion and Future work

6.1 Conclusion

To conclude the discussion, we can say SPR technology has advancements and it is becoming a reliable option for bio-sensors. PCF based SPR sensors are preferred for their convenient bio-analyte sensing and bio recognition methods. Also, SPR based PCF sensors are easy to fabricate than others and doesn't require labels of samples. Also, remotely real time monitoring is a reason to choose SPR based PCF sensors. Propagation of light can be controlled by the changing of parameters.

Our design is also an SPR based PCF sensor which is trigonal cluster-based structure. A PML layer was used outside for not allowing energy absorption from outside and inside. Plasmonic material Gold was chosen because it has low loss and is chemically stable. The results were satisfactory in case of performance parameters discussed above. We also proposed temperature sensing using Ethanol as analyte and magnetic field sensing using Magnetic Fluid as analyte respectively. In these environmental parameters detection, the sensor showed satisfactory results too. This sensor was a multipurpose highly sensitive sensor as our we aimed.

6.2 Future work

Our future work includes a various analysis of performance parameters. We aim for increasing the sensing range and sensitivity using less complicated fabrication sensors. This includes-

- Analysis of different plasmonic materials

- Analysis of different PCF structures
- Analysis of temperature, strain and magnetic detection with other materials
- Using two/three plasmonic materials.
- Increasing the sensing range and as well as sensitivity
- Implementing fabrication friendly sensors.

References

[1] S. Chowdhury *et al.*, “Porous shaped photonic crystal fiber with strong confinement field in sensing applications: Design and analysis,” *Sens. Bio-Sensing Res.*, vol. 13, pp. 63–69, 2017, doi: 10.1016/j.sbsr.2017.03.002.

[2] S. Sen, S. Chowdhury, K. Ahmed, and S. Asaduzzaman, “Design of a porous cored hexagonal photonic crystal fiber based optical sensor with high relative sensitivity for lower operating wavelength,” *Photonic Sensors*, vol. 7, no. 1, pp. 55–65, 2017, doi: 10.1007/s13320-016-0384-y.

[3] “Fiber optic sensing: The past, present, and exciting future - Sensuron.” https://www.sensuron.com/press/fiber-optic-sensing-the-past-present-and-exciting-future/ (accessed May 13, 2022).

[4] R. Stoltenburg, C. Reinemann, and B. Strehlitz, “SELEX—A (r)evolutionary method to generate high-affinity nucleic acid ligands,” *Biomol. Eng.*, vol. 24, no. 4, pp. 381–403, Oct. 2007, doi: 10.1016/j.bioeng.2007.06.001.

[5] Y. Saylan and A. Denizli, “Chapter 1 - Fundamentals and Applications of Molecularly Imprinted Systems,” in *Molecular Imprinting for Nanosensors and Other Sensing Applications*, A. Denizli, Ed. Elsevier, 2021, pp. 1–17.

[6] E. K. Akowuah, T. Gorman, H. Ademgil, S. Haxha, G. K. Robinson, and J. V Oliver, “Numerical analysis of a photonic crystal fiber for biosensing applications,” *IEEE J. Quantum Electron.*, vol. 48, no. 11, pp. 1403–1410, 2012, doi: 10.1109/JQE.2012.2213803.

[7] J. Ortega-Mendoza, A. Padilla-Vivanco, C. Toxqui-Quitl, P. Zaca-Morán, D. Villegas-Hernández, and F. Chávez, “Optical Fiber Sensor Based on Localized Surface Plasmon Resonance Using Silver Nanoparticles Photodeposited on the Optical Fiber End,” *Sensors*, vol. 14, no. 10, pp. 18701–18710, Oct. 2014, doi: 10.3390/s141018701.

[8] R. Otupiri, E. K. Akowuah, S. Haxha, H. Ademgil, F. AbdelMalek, and A. Aggoun, “A

Novel Birefrigent Photonic Crystal Fiber Surface Plasmon Resonance Biosensor," *IEEE Photonics J.*, vol. 6, no. 4, pp. 1–11, Aug. 2014, doi: 10.1109/JPHOT.2014.2335716.

[9] B. Liedberg, C. Nylander, and I. Lunström, "Surface plasmon resonance for gas detection and biosensing," *Sensors and Actuators*, vol. 4, pp. 299–304, Jan. 1983, doi: 10.1016/0250-6874(83)85036-7.

[10] E. Kretschmann and H. Raether, "Notizen: Radiative Decay of Non Radiative Surface Plasmons Excited by Light," *Zeitschrift für Naturforsch. A*, vol. 23, no. 12, pp. 2135–2136, Dec. 1968, doi: 10.1515/zna-1968-1247.

[11] M. R. Islam *et al.*, "Trigonal cluster-based ultra-sensitive surface plasmon resonance sensor for multipurpose sensing," *Sens. Bio-Sensing Res.*, vol. 35, p. 100477, 2022, doi: https://doi.org/10.1016/j.sbsr.2022.100477.

[12] S. I. Azzam, M. F. O. Hameed, R. E. A. Shehata, A. M. Heikal, and S. S. A. Obayya, "Multichannel photonic crystal fiber surface plasmon resonance based sensor," *Opt. Quantum Electron.*, vol. 48, no. 2, p. 142, Feb. 2016, doi: 10.1007/s11082-016-0414-4.

[13] M. R. Islam, M. F. Kabir, K. M. A. Talha, and M. S. Islam, "A novel hollow core terahertz refractometric sensor," *Sens. Bio-Sensing Res.*, vol. 25, p. 100295, Sep. 2019, doi: 10.1016/j.sbsr.2019.100295.

[14] F. A. Mou, M. M. Rahman, M. R. Islam, and M. I. H. Bhuiyan, "Development of a photonic crystal fiber for THz wave guidance and environmental pollutants detection," *Sens. Bio-Sensing Res.*, vol. 29, p. 100346, Aug. 2020, doi: 10.1016/j.sbsr.2020.100346.

[15] M. S. Islam, M. R. Islam, J. Sultana, A. Dinovitser, B. W.-H. Ng, and D. Abbott, "Exposed-core localized surface plasmon resonance biosensor," *J. Opt. Soc. Am. B*, vol. 36, no. 8, p. 2306, Aug. 2019, doi: 10.1364/josab.36.002306.

[16] J. N. Dash and R. Jha, "SPR Biosensor Based on Polymer PCF Coated With Conducting Metal Oxide," *IEEE Photonics Technol. Lett.*, vol. 26, no. 6, pp. 595–598, Mar. 2014, doi: 10.1109/LPT.2014.2301153.

[17] A. A. Rifat, R. Ahmed, G. A. Mahdiraji, and F. R. M. Adikan, "Highly Sensitive D-Shaped Photonic Crystal Fiber-Based Plasmonic Biosensor in Visible to Near-IR," *IEEE*

Sens. J., vol. 17, no. 9, pp. 2776–2783, May 2017, doi: 10.1109/JSEN.2017.2677473.

[18] S. Sharmin, A. Bosu, and S. Akter, “A Simple Gold-Coated Photonic Crystal Fiber Based Plasmonic Biosensor,” in *2018 International Conference on Advancement in Electrical and Electronic Engineering (ICAEEE)*, Nov. 2018, pp. 1–4, doi: 10.1109/ICAEEE.2018.8643003.

[19] J. C. Knight, “Photonic crystal fibres,” *Nature*, vol. 424, no. 6950, pp. 847–851, 2003, doi: 10.1038/nature01940.

[20] T. A. Birks, P. J. Roberts, P. S. T. J. Russell, D. M. Atkin, and T. J. Shepherd, “Full 2-D photonic bandgaps in silica/air structures,” *Electron. Lett.*, vol. 31, no. 22, pp. 1941–1943, Oct. 1995, doi: 10.1049/EL:19951306.

[21] J. C. Knight, T. A. Birks, P. S. J. Russell, and D. M. Atkin, “All-silica single-mode optical fiber with photonic crystal cladding,” *Opt. Lett.*, vol. 21, no. 19, pp. 1547–1549, Oct. 1996, doi: 10.1364/OL.21.001547.

[22] “Fundamentals of Optical Fibers, 2nd Edition - NASA/ADS.” https://ui.adsabs.harvard.edu/abs/2004fof..book.....B/abstract (accessed May 13, 2022).

[23] K. Kaneshima, Y. Namihira, N. Zou, H. Higa, and Y. Nagata, “Numerical Investigation of Octagonal Photonic Crystal Fibers with Strong Confinement Field,” *IEICE Trans.*, vol. 89–C, pp. 830–837, 2006, doi: 10.1093/ietele/e89-c.6.830.

[24] J. C. Knight, J. Broeng, T. A. Birks, and P. S. J. Russell, “Photonic Band Gap Guidance in Optical Fibers,” *Science (80-.).*, vol. 282, no. 5393, pp. 1476–1478, 1998, doi: 10.1126/science.282.5393.1476.

[25] K. Tajima, K. Kurokawa, K. Nakajima, and I. Sankawa, “Photonic crystal fiber,” *NTT Tech. Rev.*, vol. 3, no. 8, pp. 57–61, 2005, doi: 10.1126/science.1079280.

[26] A. M. Cubillas *et al.*, “Photonic crystal fibres for chemical sensing and photochemistry,” *Chem. Soc. Rev.*, vol. 42, no. 22, pp. 8629–8648, 2013, doi: 10.1039/c3cs60128e.

[27] J. Lægsgaard, N. A. Mortensen, and A. Bjarklev, “Mode areas and field-energy distribution in honeycomb photonic bandgap fibers,” *J. Opt. Soc. Am. B*, vol. 20, no. 10, p.

2037, 2003, doi: 10.1364/josab.20.002037.

[28] P. S. Maji and P. R. Chaudhuri, “Geometrical parameters dependence towards ultra-flat dispersion square-lattice PCF using tunable liquid infiltration,” *WRAP 2013 - Work. Recent Adv. Photonics*, vol. 2, no. D, pp. 2–3, 2014, doi: 10.1109/WRAP.2013.6917653.

[29] R. Islam, M. S. Habib, G. K. M. Hasanuzzaman, S. Rana, M. A. Sadath, and C. Markos, “A Novel Low-Loss Diamond-Core Porous Fiber for Polarization Maintaining Terahertz Transmission,” *IEEE Photonics Technol. Lett.*, vol. 28, no. 14, pp. 1537–1540, 2016, doi: 10.1109/LPT.2016.2550205.

[30] K. Ahmed and M. Morshed, “Design and numerical analysis of microstructured-core octagonal photonic crystal fiber for sensing applications,” *Sens. Bio-Sensing Res.*, vol. 7, pp. 1–6, Mar. 2016, doi: 10.1016/j.sbsr.2015.10.005.

[31] S. Li, “Equiangular spiral photonic crystal fiber for code synchronization in all-optical analog-to-digital conversion based on lumped time delay compensation scheme,” *Optik (Stuttg).*, vol. 127, no. 11, pp. 4693–4697, 2016, doi: 10.1016/j.ijleo.2016.02.017.

[32] A. Cerqueira S., Jr., C. M. B. Cordeiro, F. Biancalana, P. J. Roberts, H. E. Hernandez-Figueroa, and C. H. B. Cruz, “Nonlinear interaction between two different photonic bandgaps of a hybrid photonic crystal fiber,” *Opt. Lett.*, vol. 33, no. 18, p. 2080, 2008, doi: 10.1364/ol.33.002080.

[33] J. Canning, E. Buckley, K. Lyttikainen, and T. Ryan, “Wavelength dependent leakage in a Fresnel-based air-silica structured optical fibre,” *Opt. Commun.*, vol. 205, no. 1–3, pp. 95–99, 2002, doi: 10.1016/S0030-4018(02)01305-6.

[34] X. Tao, *Wearable photonics based on integrative polymeric photonic fibres*. Woodhead Publishing Limited, 2005.

[35] Y. Wang, “Review of long period fiber gratings written by CO2 laser,” *J. Appl. Phys.*, vol. 108, no. 8, 2010, doi: 10.1063/1.3493111.

[36] H. F. Fakhruldeen and A. Z. Ghazi Zahid, “An Overview of Photonic Crystal Fiber (PCF),” no. April 2019, 2019, [Online]. Available: www.tnsroindia.org.in.

[37] V. V. R. K. Kumar *et al.*, “Extruded soft glass photonic crystal fiber for ultrabroad supercontinuum generation,” *Opt. Express*, vol. 10, no. 25, pp. 1520–1525, Dec. 2002, doi: 10.1364/OE.10.001520.

[38] D. M. Chow, S. R. Sandoghchi, and F. R. M. Adikan, “Fabrication of photonic crystal fibers,” *ICP 2012 - 3rd Int. Conf. Photonics 2012, Proc.*, no. October, pp. 227–230, 2012, doi: 10.1109/ICP.2012.6379830.

[39] J.-C. Kim, H.-K. Kim, U.-C. Paek, B.-H. Lee, and J.-B. Eom, “The Fabrication of a Photonic Crystal Fiber and Measurement of its Properties,” *J. Opt. Soc. Korea*, vol. 7, no. 2, pp. 79–83, Jun. 2003, doi: 10.3807/JOSK.2003.7.2.079.

[40] “Max Planck Institute for the Science of Light.” https://mpl.mpg.de/research-at-mpl/technology-development-service-units/tdsu-fibre-fabrication-glass-studio/research/fibre-fabrication/stack-and-draw/]. (accessed May 13, 2022).

[41] S. Zeng, D. Baillargeat, H. P. Ho, and K. T. Yong, “Nanomaterials enhanced surface plasmon resonance for biological and chemical sensing applications,” *Chem. Soc. Rev.*, vol. 43, no. 10, pp. 3426–3452, 2014, doi: 10.1039/c3cs60479a.

[42] J. B. González-Díaz *et al.*, “Plasmonic Au/Co/Au nanosandwiches with enhanced magneto-optical activity,” *Small*, vol. 4, no. 2, pp. 202–205, 2008, doi: 10.1002/smll.200700594.

[43] G. X. Du, T. Mori, M. Suzuki, S. Saito, H. Fukuda, and M. Takahashi, “Evidence of localized surface plasmon enhanced magneto-optical effect in nanodisk array,” *Appl. Phys. Lett.*, vol. 96, no. 8, pp. 2008–2011, 2010, doi: 10.1063/1.3334726.

[44] S. Zeng *et al.*, “Size dependence of Au NP-enhanced surface plasmon resonance based on differential phase measurement,” *Sensors Actuators, B Chem.*, vol. 176, pp. 1128–1133, 2013, doi: 10.1016/j.snb.2012.09.073.

[45] Y. Yanase *et al.*, “Surface plasmon resonance for cell-based clinical diagnosis,” *Sensors (Switzerland)*, vol. 14, no. 3, pp. 4948–4959, 2014, doi: 10.3390/s140304948.

[46] *Surface plasmon wave*, vol. 266. 2016.

[47] “Nanoplasmonics and Three-Dimensional Plasmonic Metamaterials | NIST.” https://www.nist.gov/programs-projects/nanoplasmonics-and-three-dimensional-plasmonic-metamaterials (accessed May 13, 2022).

[48] E. Descrovi, V. Paeder, L. Vaccaro, and H.-P. Herzig, “A virtual optical probe based on localized Surface Plasmon Polaritons,” *Opt. Express*, vol. 13, no. 18, p. 7017, 2005, doi: 10.1364/opex.13.007017.

[49] K. Y. Bliokh, F. J. Rodríguez-Fortuño, A. Y. Bekshaev, Y. S. Kivshar, and F. Nori, “Electric-current-induced unidirectional propagation of surface plasmon-polaritons,” *Opt. Lett.*, vol. 43, no. 5, p. 963, 2018, doi: 10.1364/ol.43.000963.

[50] M. V. Bashevoy, F. Jonsson, A. V. Krasavin, N. I. Zheludev, Y. Chen, and M. I. Stockman, “Generation of traveling surface plasmon waves by free-electron impact,” *Nano Lett.*, vol. 6, no. 6, pp. 1113–1115, 2006, doi: 10.1021/nl060941v.

[51] “Surface plasmon polariton - Wikipedia.” https://en.wikipedia.org/wiki/Surface_plasmon_polariton (accessed May 13, 2022).

[52] “Evanescent field - Wikipedia.” https://en.wikipedia.org/wiki/Evanescent_field (accessed May 13, 2022).

[53] X. Yu *et al.*, “A selectively coated photonic crystal fiber based surface plasmon resonance sensor,” *J. Opt.*, vol. 12, no. 1, p. 15005, Jan. 2010, doi: 10.1088/2040-8978/12/1/015005.

[54] H. Minh Hiep *et al.*, “A localized surface plasmon resonance based immunosensor for the detection of casein in milk,” *Sci. Technol. Adv. Mater.*, vol. 8, no. 4, pp. 331–338, 2007, doi: 10.1016/j.stam.2006.12.010.

[55] A. Sinibaldi *et al.*, “Direct comparison of the performance of Bloch surface wave and surface plasmon polariton sensors,” *Sensors Actuators, B Chem.*, vol. 174, pp. 292–298, 2012, doi: 10.1016/j.snb.2012.07.015.

[56] S. Pillai, K. R. Catchpole, T. Trupke, and M. A. Green, “Surface plasmon enhanced silicon solar cells,” *J. Appl. Phys.*, vol. 101, no. 9, 2007, doi: 10.1063/1.2734885.

[57] K. Locharoenrat, H. Sano, and G. Mizutani, “Phenomenological studies of optical

properties of Cu nanowires," *Sci. Technol. Adv. Mater.*, vol. 8, no. 4, pp. 277–281, 2007, doi: 10.1016/j.stam.2007.02.001.

[58] W. Knoll, "Interfaces and thin films as seen by bound electromagnetic waves," *Annu. Rev. Phys. Chem.*, vol. 49, no. 1, pp. 569–638, 1998, doi: 10.1146/annurev.physchem.49.1.569.

[59] D. J. J. Hu and H. P. Ho, "Recent advances in plasmonic photonic crystal fibers: design, fabrication and applications," *Adv. Opt. Photonics*, vol. 9, no. 2, p. 257, 2017, doi: 10.1364/aop.9.000257.

[60] K. Bhattarai *et al.*, "A Large-Area, Mushroom-Capped Plasmonic Perfect Absorber: Refractive Index Sensing and Fabry–Perot Cavity Mechanism," *Adv. Opt. Mater.*, vol. 3, no. 12, pp. 1779–1786, 2015, doi: https://doi.org/10.1002/adom.201500231.

[61] M. R. Momota and M. R. Hasan, "Hollow-core silver coated photonic crystal fiber plasmonic sensor," *Opt. Mater. (Amst).*, vol. 76, pp. 287–294, Feb. 2018, doi: 10.1016/j.optmat.2017.12.049.

[62] Y. Zhao, Z. Q. Deng, and J. Li, "Photonic crystal fiber based surface plasmon resonance chemical sensors," *Sensors Actuators, B Chem.*, vol. 202, pp. 557–567, 2014, doi: 10.1016/j.snb.2014.05.127.

[63] M. S. Islam *et al.*, "A Hi-Bi Ultra-Sensitive Surface Plasmon Resonance Fiber Sensor," *IEEE Access*, vol. 7, no. June, pp. 79085–79094, 2019, doi: 10.1109/ACCESS.2019.2922663.

[64] N. Luan, R. Wang, W. Lv, and J. Yao, "Surface plasmon resonance sensor based on D-shaped microstructured optical fiber with hollow core," *Opt. Express*, vol. 23, no. 7, p. 8576, Apr. 2015, doi: 10.1364/OE.23.008576.

[65] X. Chen, L. Xia, and C. Li, "Surface plasmon resonance sensor based on a novel D-shaped photonic crystal fiber for low refractive index detection," *IEEE Photonics J.*, vol. 10, no. 1, 2018, doi: 10.1109/JPHOT.2018.2790424.

[66] E. Haque, M. A. Hossain, F. Ahmed, and Y. Namihira, "Surface Plasmon Resonance Sensor Based on Modified D-Shaped Photonic Crystal Fiber for Wider Range of Refractive Index Detection," *IEEE Sens. J.*, vol. 18, no. 20, pp. 8287–8293, 2018, doi:

10.1109/JSEN.2018.2865514.

[67] E. Haque, A. Al Noman, M. A. Hossain, N. Hoang Hai, Y. Namihira, and F. Ahmed, “Highly Sensitive D-Shaped Plasmonic Refractive Index Sensor for a Broad Range of Refractive Index Detection,” *IEEE Photonics J.*, vol. 13, no. 1, pp. 1–11, Feb. 2021, doi: 10.1109/JPHOT.2021.3055234.

[68] M. F. H. Arif, M. M. Hossain, N. Islam, and S. M. Khaled, “A nonlinear photonic crystal fiber for liquid sensing application with high birefringence and low confinement loss,” *Sens. Bio-Sensing Res.*, vol. 22, no. November 2018, p. 100252, 2019, doi: 10.1016/j.sbsr.2018.100252.

[69] S. Sen, M. Abdullah-Al-Shafi, and M. A. Kabir, “Hexagonal photonic crystal Fiber (H-PCF) based optical sensor with high relative sensitivity and low confinement loss for terahertz (THz) regime,” *Sens. Bio-Sensing Res.*, vol. 30, no. September, p. 100377, 2020, doi: 10.1016/j.sbsr.2020.100377.

[70] A. A. Rifat, G. A. Mahdiraji, Y. G. Shee, M. J. Shawon, and F. R. M. Adikan, “A Novel Photonic Crystal Fiber Biosensor Using Surface Plasmon Resonance,” *Procedia Eng.*, vol. 140, pp. 1–7, 2016, doi: 10.1016/j.proeng.2015.08.1107.

[71] M. Mahabubur Rahman, M. Aslam Molla, A. Kumar Paul, M. A. Based, M. Masud Rana, and M. S. Anower, “Numerical investigation of a highly sensitive plasmonic refractive index sensor utilizing hexagonal lattice of photonic crystal fiber,” *Results Phys.*, vol. 18, p. 103313, 2020, doi: 10.1016/j.rinp.2020.103313.

[72] T. Ahmed, A. K. Paul, M. S. Anower, and S. M. A. Razzak, “Surface plasmon resonance biosensor based on hexagonal lattice dual-core photonic crystal fiber,” *Appl. Opt.*, vol. 58, no. 31, pp. 8416–8422, Nov. 2019, doi: 10.1364/AO.58.008416.

[73] H. Wang, X. Yan, S. Li, G. An, and X. Zhang, “High sensitivity refractive index sensor based on dual-core photonic crystal fiber with hexagonal lattice,” *Sensors (Switzerland)*, vol. 16, no. 10, pp. 1–10, 2016, doi: 10.3390/s16101655.

[74] S. M. Abu Sufian Sunny, T. Ahmed, A. Anzum, and A. K. Paul, “Performance Analysis of a PCF SPR Based Highly Sensitive Biosensor,” *BECITHCON 2019 - 2019 IEEE Int.*

Conf. Biomed. Eng. Comput. Inf. Technol. Heal., no. Cvd, pp. 7–10, 2019, doi: 10.1109/BECITHCON48839.2019.9063192.

[75] M. R. Hasan, S. Akter, A. A. Rifat, S. Rana, and S. Ali, "A highly sensitive gold-coated photonic crystal fiber biosensor based on surface plasmon resonance," *Photonics*, vol. 4, no. 1, Mar. 2017, doi: 10.3390/photonics4010018.

[76] M. A. Khalek, S. Chakma, B. K. Paul, and K. Ahmed, "Dataset of surface plasmon resonance based on photonic crystal fiber for chemical sensing applications," *Data Br.*, vol. 19, pp. 76–81, 2018, doi: 10.1016/j.dib.2018.05.026.

[77] Q. M. Kamrunnahar, J. R. Mou, and M. Momtaj, "Dual-core gold coated photonic crystal fiber plasmonic sensor: Design and analysis," *Results Phys.*, vol. 18, no. June, p. 103319, 2020, doi: 10.1016/j.rinp.2020.103319.

[78] M. Hossain, S. M. A. S. Sunny, and T. Ahmed, "Design and Analysis of Circular Lattice PCF Biosensor -Based on Surface Plasmon Resonance," in *2021 3rd International Conference on Sustainable Technologies for Industry 4.0 (STI)*, 2021, pp. 1–4, doi: 10.1109/STI53101.2021.9732610.

[79] M. S. Islam, J. Sultana, A. Dinovitser, B. W.-H. Ng, and D. Abbott, "A Gold Coated Plasmonic Sensor for Biomedical and Biochemical Analyte Detection," in *2018 43rd International Conference on Infrared, Millimeter, and Terahertz Waves (IRMMW-THz)*, Sep. 2018, pp. 1–2, doi: 10.1109/IRMMW-THz.2018.8510018.

[80] S. Chu, K. Nakkeeran, A. M. Abobaker, S. S. Aphale, P. R. Babu, and K. Senthilnathan, "Design and analysis of surface-plasmon-resonance-based photonic quasi-crystal fiber biosensor for high-refractive-index liquid analytes," *IEEE J. Sel. Top. Quantum Electron.*, vol. 25, no. 2, pp. 1–8, Mar. 2019, doi: 10.1109/JSTQE.2018.2873481.

[81] M. N. Hossen, M. Ferdous, M. Abdul Khalek, S. Chakma, B. K. Paul, and K. Ahmed, "Design and analysis of biosensor based on surface plasmon resonance," *Sens. Bio-Sensing Res.*, vol. 21, pp. 1–6, Nov. 2018, doi: 10.1016/j.sbsr.2018.08.003.

[82] M. R. Hasan *et al.*, "Spiral photonic crystal fiber-based dual-polarized surface plasmon resonance biosensor," *IEEE Sens. J.*, vol. 18, no. 1, pp. 133–140, Jan. 2018, doi:

10.1109/JSEN.2017.2769720.

[83] P. R. West, S. Ishii, G. Naik, N. Emani, V. M. Shalaev, and A. Boltasseva, “Searching for Better Plasmonic Materials.”

[84] M. Alsawafta, M. Wahbeh, and V. Van Truong, “Plasmonic modes and optical properties of gold and silver ellipsoidal nanoparticles by the discrete dipole approximation,” *J. Nanomater.*, vol. 2012, 2012, doi: 10.1155/2012/457968.

[85] G. V Naik, V. M. Shalaev, and A. Boltasseva, “Alternative Plasmonic Materials: Beyond Gold and Silver,” *Adv. Mater.*, vol. 25, no. 24, pp. 3264–3294, Jun. 2013, doi: 10.1002/adma.201205076.

[86] M. K. Hamza *et al.*, “Tunable mid IR plasmon in GZO nanocrystals,” *Nanoscale*, vol. 7, no. 28, pp. 12030–12037, 2015, doi: 10.1039/C5NR03378K.

[87] “Five reasons why glass is best for medical devices | SCHOTT.” https://www.schott.com/en-gb/products/p/puravis/content/five-reasons-why-glass-is-best-for-medical-devices (accessed May 13, 2022).

[88] F. Haider, R. A. Aoni, R. Ahmed, G. A. Mahdiraji, M. F. Azman, and F. R. M. Adikan, “Mode-multiplex plasmonic sensor for multi-analyte detection,” *Opt. Lett.*, vol. 45, no. 14, pp. 3945–3948, Jul. 2020, doi: 10.1364/OL.396340.

[89] A. M. Shrivastav, U. Cvelbar, and I. Abdulhalim, “A comprehensive review on plasmonic-based biosensors used in viral diagnostics,” *Commun. Biol.*, vol. 4, no. 1, pp. 1–12, 2021, doi: 10.1038/s42003-020-01615-8.

[90] M. R. Islam *et al.*, “Design and Analysis of a Biochemical Sensor Based on Surface Plasmon Resonance with Ultra-high Sensitivity,” *Plasmonics*, Jan. 2021, doi: 10.1007/s11468-020-01355-9.

[91] M. Rakibul Islam, M. M. I. Khan, F. Mehjabin, J. Alam Chowdhury, and M. Islam, “Design of a fabrication friendly & highly sensitive surface plasmon resonance-based photonic crystal fiber biosensor,” *Results Phys.*, vol. 19, p. 103501, Dec. 2020, doi: 10.1016/j.rinp.2020.103501.

[92] M. Aminul Islam, M. Rakibul Islam, M. Moinul Islam Khan, J. A. Chowdhury, F. Mehjabin, and M. Islam, “Highly Birefringent Slotted Core Photonic Crystal Fiber for THz Wave Propagation,” *Phys. Wave Phenom.*, vol. 28, no. 1, pp. 58–67, Jan. 2020, doi: 10.3103/S1541308X20010021.

[93] M. R. Islam *et al.*, “Design and analysis of birefringent SPR based PCF biosensor with ultra-high sensitivity and low loss,” *Optik (Stuttg).*, vol. 221, p. 165311, Nov. 2020, doi: 10.1016/j.ijleo.2020.165311.

[94] X. Li, S. Li, X. Yan, D. Sun, Z. Liu, and T. Cheng, “High Sensitivity Photonic Crystal Fiber Refractive Index Sensor with Gold Coated Externally Based on Surface Plasmon Resonance,” 2018, doi: 10.3390/mi9120640.

[95] C. Liu *et al.*, “Symmetrical dual D-shape photonic crystal fibers for surface plasmon resonance sensing,” *Opt. Express*, vol. 26, no. 7, p. 9039, Apr. 2018, doi: 10.1364/OE.26.009039.

[96] M. Al Mahfuz, M. A. Hossain, E. Haque, N. H. Hai, Y. Namihira, and F. Ahmed, “Dual-Core Photonic Crystal Fiber-Based Plasmonic RI Sensor in the Visible to Near-IR Operating Band,” *IEEE Sens. J.*, vol. 20, no. 14, pp. 7692–7700, Mar. 2020, doi: 10.1109/jsen.2020.2980327.

[97] M. R. Islam *et al.*, “Design and numerical analysis of a gold-coated photonic crystal fiber based refractive index sensor,” *Opt. Quantum Electron.*, vol. 53, no. 2, p. 112, Feb. 2021, doi: 10.1007/s11082-021-02748-8.

[98] E. Haque, M. Anwar Hossain, Y. Namihira, and F. Ahmed, “Microchannel-based plasmonic refractive index sensor for low refractive index detection,” *Appl. Opt.*, vol. 58, no. 6, p. 1547, Feb. 2019, doi: 10.1364/AO.58.001547.

[99] M. S. Islam *et al.*, “Localized surface plasmon resonance biosensor: an improved technique for SERS response intensification,” *Opt. Lett.*, vol. 44, no. 5, p. 1134, Mar. 2019, doi: 10.1364/ol.44.001134.

[100] M. R. Islam *et al.*, “Surface plasmon resonance based highly sensitive gold coated PCF biosensor,” *Appl. Phys. A*, vol. 127, no. 2, p. 118, Feb. 2021, doi: 10.1007/s00339-020-

04162-5.

[101] Y. Yu *et al.*, “Some features of the photonic crystal fiber temperature sensor with liquid ethanol filling,” *Opt. Express*, vol. 18, no. 15, pp. 15383–15388, Jul. 2010, doi: 10.1364/OE.18.015383.

[102] S. Liu, S. Cao, Z. Zhang, Y. Wang, C. Liao, and Y. Wang, “Temperature Sensor Based on Side-Polished Fiber SPR Device Coated with Polymer,” *Sensors*, vol. 19, no. 19, p. 4063, Sep. 2019, doi: 10.3390/s19194063.

[103] M. R. Islam *et al.*, “Design and analysis of a QC-SPR-PCF sensor for multipurpose sensing with supremely high FOM,” *Appl. Nanosci.*, vol. 12, no. 1, pp. 29–45, 2022, doi: 10.1007/s13204-021-02150-6.

[104] X. Zhou *et al.*, “High-Sensitivity SPR Temperature Sensor Based on Hollow-Core Fiber,” *IEEE Trans. Instrum. Meas.*, vol. 69, no. 10, pp. 8494–8499, 2020, doi: 10.1109/TIM.2020.2992828.

[105] Y. Wang, Q. Huang, W. Zhu, M. Yang, and E. Lewis, “Novel optical fiber SPR temperature sensor based on MMF-PCF-MMF structure and gold-PDMS film,” *Opt. Express*, vol. 26, no. 2, p. 1910, 2018, doi: 10.1364/oe.26.001910.

[106] M. A. Mollah, S. M. R. Islam, M. Yousufali, L. F. Abdulrazak, M. B. Hossain, and I. S. Amiri, “Plasmonic temperature sensor using D-shaped photonic crystal fiber,” *Results Phys.*, vol. 16, p. 102966, Mar. 2020, doi: 10.1016/j.rinp.2020.102966.

[107] J. N. Dash and R. Das, “SPR based magnetic-field sensing in microchannelled PCF: a numerical approach,” *J. Opt.*, vol. 20, no. 11, p. 115001, Nov. 2018, doi: 10.1088/2040-8986/aae119.

[108] Y. Zhao, X. Liu, R.-Q. Lv, Y.-N. Zhang, and Q. Wang, “Review on Optical Fiber Sensors Based on the Refractive Index Tunability of Ferrofluid,” *J. Light. Technol.*, vol. 35, no. 16, pp. 3406–3412, Aug. 2017, doi: 10.1109/JLT.2016.2573288.

[109] H. Huang *et al.*, “A Highly Magnetic Field Sensitive Photonic Crystal Fiber Based on Surface Plasmon Resonance,” *Sensors*, vol. 20, no. 18, p. 5193, Sep. 2020, doi: 10.3390/s20185193.

[110] R. Zhang *et al.*, “Mach-Zehnder Interferometer Cascaded With FBG for Simultaneous Measurement of Magnetic Field and Temperature,” *IEEE Sens. J.*, vol. 19, no. 11, pp. 4079–4083, 2019, doi: 10.1109/JSEN.2019.2899672.

[111] J. Wang *et al.*, “Magnetic field and temperature dual-parameter sensor based on magnetic fluid materials filled photonic crystal fiber,” *Opt. Express*, vol. 28, no. 2, pp. 1456–1471, Jan. 2020, doi: 10.1364/OE.377116.

[112] X. Mo, J. Lv, Q. Liu, X. Jiang, and G. Si, “A Magnetic Field SPR Sensor Based on Temperature Self-Reference,” *Sensors*, vol. 21, no. 18, 2021, doi: 10.3390/s21186130.

[113] S. W. Sijun Weng, L. P. Li Pei, J. W. Jianshuai Wang, T. N. Tigang Ning, and and J. L. and Jing Li, “High sensitivity side-hole fiber magnetic field sensor based on surface plasmon resonance,” *Chinese Opt. Lett.*, vol. 14, no. 11, pp. 110603–110606, 2016, doi: 10.3788/COL201614.110603.

[114] G. A. Mahdiraji *et al.*, “Challenges and solutions in fabrication of silica-based photonic crystal fibers: An experimental study,” *Fiber Integr. Opt.*, vol. 33, no. 1–2, pp. 85–104, 2014, doi: 10.1080/01468030.2013.879680.

[115] G. S. Wiederhecker *et al.*, “Field enhancement within an optical fibre with a subwavelength air core,” *Nat. Photonics*, vol. 1, no. 2, pp. 115–118, 2007, doi: 10.1038/nphoton.2006.81.

[116] B. Li, T. Cheng, J. Chen, and X. Yan, “Graphene-Enhanced Surface Plasmon Resonance Liquid Refractive Index Sensor Based on Photonic Crystal Fiber,” *Sensors*, vol. 19, no. 17, 2019, doi: 10.3390/s19173666.

[117] E. Haque, A. Al Noman, M. A. Hossain, N. Hoang Hai, Y. Namihira, and F. Ahmed, “Highly sensitive D-Shaped plasmonic refractive index sensor for a broad range of refractive index detection,” *IEEE Photonics J.*, vol. 13, no. 1, 2021, doi: 10.1109/JPHOT.2021.3055234.

[118] E. Delory and J. Pearlman, Eds., “Chapter 3 - Ocean In Situ Sensors: New Developments in Biological Sensors,” in *Challenges and Innovations in Ocean In Situ Sensors*, Elsevier, 2019, pp. 81–116.

[119] H.-W. Yu, M. J. Halonen, and I. L. Pepper, “Chapter 12 - Immunological Methods,” in *Environmental Microbiology (Third Edition)*, Third Edit., I. L. Pepper, C. P. Gerba, and T. J. Gentry, Eds. San Diego: Academic Press, 2015, pp. 245–269.

[120] J. Dostálek and W. Knoll, “2.26 - Plasmonics,” in *Polymer Science: A Comprehensive Reference*, K. Matyjaszewski and M. Möller, Eds. Amsterdam: Elsevier, 2012, pp. 647–659.

[121] H. Yoo, J. Shin, J. Sim, H. Cho, and S. Hong, “Biosensors and Bioelectronics Reusable surface plasmon resonance biosensor chip for the detection of H1N1 influenza virus,” *Biosens. Bioelectron.*, vol. 168, no. March, p. 112561, 2020, doi: 10.1016/j.bios.2020.112561.

[122] K. Zhang and M. Rochette, “Saturable absorption using nonlinear multimode interference in chalcogenide fiber,” in *OSA Advanced Photonics Congress (AP) 2020 (IPR, NP, NOMA, Networks, PVLED, PSC, SPPCom, SOF)*, 2020, p. NpM3E.3, doi: 10.1364/NP.2020.NpM3E.3.

Publication

i. M. R. Islam *et al.*, “Trigonal cluster-based ultra-sensitive surface plasmon resonance sensor for multipurpose sensing,” *Sens. Bio-Sensing Res.*, vol. 35, p. 100477, 2022, doi: https://doi.org/10.1016/j.sbsr.2022.100477